Reflectance and hydrated materials of Vesta: Investigation of their variations and relationship using an improved calibration of Dawn VIR mapping spectrometer

Jean-Philippe Combe[1], Eleonora Ammannito[2,3], Federico Tosi[2], Maria Cristina de Sanctis[2], Thomas B. McCord[1], Carol A. Raymond[4], Christopher T. Russell[3]

[1]Bear Fight Institute, 22 Fiddler's Road, P.O. Box 667, Winthrop, WA 98862, USA (jean-philippe_combe @ bearfightinstitute.com / Fax: +001-509-996-3772).

[2]Istituto di Astrofisica e Planetologia Spaziali-Istituto Nazionale di Astrofisica, Rome, Italy

[3]Institute of Geophysics and Planetary Physics, University of California Los Angeles, CA, USA

[4]Jet Propulsion Laboratory, Pasadena, CA, USA

Submitted to Icarus

Contents

Abstract

Vesta's surface albedo variations and hydrated material content share similar spatial distribution. This observation is consistent with carbonaceous chondrite meteorites as a likely source material for dark surface units observed by the Dawn spacecraft, as presented by numerous publications. While these deposits have been studied extensively by analysis of data from the Framing Camera (FC) and the Visible and Infrared Spectrometer (VIR), we performed a new analysis based on an improved calibration of VIR. First we identified instrument and calibration artifacts, and we therefore developed corrections of the VIR flat field and response function. Then we developed a photometric correction for Vesta based on the lunar model by Shkuratov et al. (1999, Icarus 141), and a semi-analytical inversion of the photometric parameters. This photometric model combines minimization of the scattering effects due to the topography (a disk function) and variations of multiple-scattering with phase angle (the phase function) caused by microscopic physical properties of the regolith. The improved calibration and photometric correction enable more accurate analysis of the spectral properties of Vesta's surface material, especially the reflectance at 1.4 μm and the 2.8 μm hydroxyl absorption band depth. We produced global and quadrangle maps that are used as a common dataset for this Icarus special issue on Vesta's surface composition. The joint interpretation of both the 1.4 μm reflectance and the 2.8 μm absorption band depth reveals unusual spectral properties for a number of impact craters and ejecta compared to the rest of Vesta. An area including the Bellicia, Arruntia and Pomponia craters, where olivine might be present, has relatively high reflectance and a strong hydroxyl absorption band. Another area in the vicinity of Capparonia crater has a high content of hydrated materials , although with moderate reflectance and typical pyroxene-rich composition. Ejecta blankets west of Oppia crater have a spectral behavior similar to Capparonia, except for the wider and more complex shape of the hydroxyl absorption band. On the other hand, some low-hydrated areas associated to crater floors and ejecta have higher reflectance and steeper spectral slope than most low-hydrated terrains Vesta. A broad lane that extends from Rheasilvia rim at Matronalia Rupes to the northern regions hosts little to no hydrated materials and exhibits a moderate spectral slope, similar to Rheasilvia's basin floor. These properties reinforce the hypothesis that the lane is composed of ejecta from Rheasilvia, as indicated by the distribution of pyroxene compositions by previous results from Dawn. A few small and fresh craters exhibit an association between low-reflectance, little to no hydrated materials and a strong positive spectral

65 slope, suggesting optical effects by opaque coatings, as opposed to carbonaceous chondrite deposits,
66 and possible coarser grains.

67 ## Highlights

68

69 • Upgrades of the flat field and response function of the VIR imaging spectrometer
70 • Phase function correction of VIR spectra between 0.4 and 3.5 μm.
71 • Global and quadrangle maps of the 1.4 μm reflectance and 2.8 μm band depth.
72 • Maps of hydrated materials and albedo reveal several types of surface units.
73

1. Introduction

The surface of asteroid 4 Vesta has been contaminated by infalling carbonaceous chondrite meteoroids, which is one result from the Dawn mission (De Sanctis et al., 2012a; McCord et al., 2012; Reddy et al., 2012; Turrini et al., 2014; Palomba et al. 2014). Vesta's regolith has a contrasted reflectance, which ranges from 7% to 30% at 0.75 μm (McCord et al., 2012). Dark materials on Vesta could be either due to carbon-rich, low-velocity impactors (exogenic), or from freshly exposed mafic material (endogenic), or impact melt (surface process) (Reddy et al., 2012; McCord et al., 2012; Palomba et al., 2014).Units below the mean reflectance are generally – but not always – correlated with hydroxyl-rich materials, which is consistent with the carbonaceous chondritic origin; they define broad areas with diffuse boundaries at regional scales from several tens to several hundreds of kilometers, or spatially-coherent and sharply contrasted units at local scales of a few kilometers or less (Reddy et al., 2012; Jaumann et al., 2014). This differs from the ubiquitous basaltic-rich nature of the native surface material of Vesta determined by visible and near-infrared spectroscopy (McCord et al., 1970; Gaffey et al., 1997; De Sanctis et al., 2012b). The link between the pyroxene-rich surface of Vesta and howardite, eucrite and diogenite meteorites (HEDs), first established from telescopic observations (McCord et al., 1970), was reinforced by observations of carbonaceous chondritic clasts in howardites (Zolensky et al., 1996; Gounelle et al., 2003; Reddy et al., 2012) which contain hydrated, hydroxylated, or oxyhydroxylated mineral phases.

The anti-correlation between surface reflectance and the 2.8 μm band depth (Fig. 1, adapted from McCord et al., 2012) is very diffuse, which indicates that more than one process have likely contributed to the composition observed today. For example the hypothesis of impact melts is relevant for low-albedo units with low hydrated content (Palomba et al., 2014). In addition, the quantities and types of hydrated phases delivered by meteoritic impacts may have been different over time (Turrini et al., 2014). Furthermore, Vesta's regolith underwent meteorite impacts that comminuted, gardened and mixed the original lithology (Pieters et al., 2012). With time, these processes homogenized the upper regolith through small-scale mixing of diverse surface components, gradually masking material exposed by impact craters, as the regolith ages, and making it fades into the background, in addition to possibly creating impact melts, altering scattering properties, destroying molecular bonds of OH and H_2O, and eventually modifying the

relationship between the surface albedo and amounts of hydrated materials. Other processes of darkening such as deposition of nanophase metallic iron from interactions of solar wind particles and micrometeoroids with the regolith, which occur on the Moon (Hapke , 2001; Noble et al., 2001), do not seem to alter significantly the optical properties of Vesta's surface, as indicated by the quasi-absence of reddening in visible-near infrared reflectance spectra (Pieters et al., 2012). Finally, the combined study of albedo and hydrated properties in McCord et al. (2012) and Turrini et al. (2014) was limited to qualitative interpretation because of calibration and photometric residuals in the data from the Visible and Infrared Mapping Spectrometer (VIR, De Sanctis et al., 2011), such as artifacts in the instrument flat-field, and incomplete correction of phase angle effects, which both created seams at the edge of each individual images projected on a map.

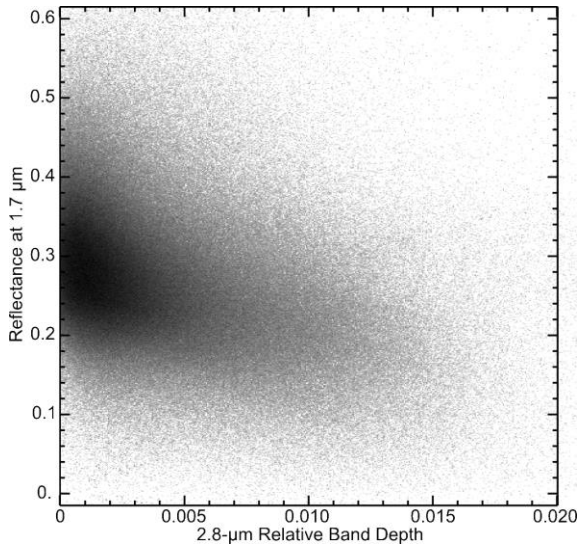

Fig. 1: Reflectance variations on Vesta and their relationship to the abundance of hydrated materials from the entire dataset of the VIR mapping spectrometer on Dawn. This two-dimension scatter plot, adapted from McCord et al. (2012), shows a linear and diffuse anti-correlation that was the first indication of a common origin for dark and hydrated materials.

Our objective is to analyze the distribution and spectral properties of Vesta's surface materials. We present maps that emphasize the significance of albedo and hydrated materials. In particular, we focus on surface units that deviate from the main linear anti-correlation trend, as a way to detect the most pure compositions and reveal some diversity that was not interpreted before. We present a new analysis of the VIR spectral dataset that includes improvements of the instrument calibration (flat field and response function), and of the photometric correction,

126 particularly the phase function. We have computed global and quadrangle maps of the 1.4 μm
127 reflectance and 2.8 μm band depth, many of which are used in this special issue of Icarus on
128 compositional mapping of Vesta by Dawn (McCord and Scully, 2015, this issue.) For improving
129 the detection and mapping of surface materials with the most pure composition, and better
130 discriminate between surface units of similar composition, we have developed a visualization
131 technique that combines the simultaneous display of two parameters, which is also used in
132 several papers of this special issue of Icarus.

133 ## 2. Data and methods for computing global maps

134 ### 2.1 Visible and Infrared Mapping Spectrometer (VIR)

135 VIR (De Sanctis et al., 2011) is an imaging spectrometer onboard the Dawn spacecraft with
136 Instantaneous field of View (IFOV) of 250 μrad/pixel and Field of View (FOV) 64×64 mrad, with
137 two push-broom detectors of 256 spatial pixels by 432 spectral pixels: one mostly sensitive to the
138 visible radiation between 0.25 and 1.07 μm (VIR VIS), and an infrared detector for the range 1.02–
139 510 μm (VIR IR), with spectral sampling of 1.8 nm and 9.8 nm respectively.
140 Dawn entered into orbit around Vesta on 16 July 2011 and departed on 5 September 2012 (Russell
141 et al., 2012). The mission was divided into four main observational phases (Table 1): Survey, High-
142 Altitude Mapping Orbit (HAMO), Low-Altitude Mapping Orbit (LAMO), and High-Altitude
143 Mapping Orbit 2 (HAMO-2). Each phase differs in duration, illumination conditions (with the phase
144 angle increasing from Survey to LAMO), and surface coverage. Only the northern polar region was
145 not observed.

146 **Table 1: Summary of VIR observations processed to create global maps of Vesta.**

Observation phase name	Observation sequence	First file number	Last file number	Number of observations	Percentage of surface covered	Average phase angle	Average incidence angle	Altitude (km)
Approach (VSA)	vir_da004_11204	364718678	364726798	7	26.2	64.6	59.4	5260
	vir_da004_11205	364759344	364830819	35	62	11.3	30.2	5246
	vir_da005_11218	365887222	365906752	30	8.1	30.8	35	2732
Survey (VSS)	vir_da006_11224	366390345	366408862	18	16.8	21	35.1	2732
	vir_da006_11227	366614355	366712455	46	39.1	46.5	50.1	2758

	vir_da007_11230	366886513	366905030	18	18.1	21.8	34.4	2733
	vir_da007_11232	367111526	367203035	32	26	49.7	51.6	2769
	vir_da008_11235	367366818	367444490	47	26.6	42.6	44.7	2754
	vir_da008_11239	367629305	367681357	44	30.3	30.1	30.9	2748
Transfer to HAMO (VTH)	vir_da009_11264	369819195	369821809	5	0.4	34.6	33.1	685
	vir_da009_11268	370219125	370221538	3	0.5	30.5	51	791
HAMO (VSH)	vir_da010_11278	370617178	371017234	40	5.5	31.2	32.6	680
	vir_da010_11279	371194617	371551412	54	5.1	29.1	58.3	780
	vir_da011_11284	371586110	371993589	70	10.2	35.6	44.9	707
	vir_da011_11289	372030376	372433939	60	10.3	30.9	42.7	724
	vir_da012_11294	372467124	372876682	68	8.6	36.8	33.9	710
	vir_da012_11299	372914324	373314339	50	5.4	36.7	38.6	673
LAMO (VSL)	vir_da017_12007	379294594	379311261	8	0.1	46.9	47.3	186
	vir_da018_12021	380500497	380517042	8	0.1	49.8	53	206
	vir_da018_12028	381103823	381120598	8	0.1	50.4	54.1	179
	vir_da019_12035	381689959	381742210	32	0.4	56.7	52.6	268
	vir_da019_12042	382309220	382360882	32	0.4	58.5	56.5	260
	vir_da020_12049	382912132	382964395	32	0.3	59.5	62	238
	vir_da020_12055	383530961	383583088	32	0.4	56.8	60.9	278
	vir_da021_12061	384150165	384201785	40	0.4	70.5	69.4	254
	vir_da021_12067	384736801	384789298	40	0.4	65.2	67.3	257
	vir_da022_12074	385355979	385407746	40	0.5	60.1	62.6	269
	vir_da022_12084	385943114	385995188	40	0.4	59.3	59.9	241
	vir_da023_12091	386530177	386596943	40	0.5	50.8	57.3	263
	vir_da023_12098	387165294	387216247	40	0.4	54.5	57.1	235
	vir_da024_12105	387720121	387771177	40	0.4	48.9	57.8	241
	vir_da024_12112	388371115	388421813	39	0.4	51.7	56.9	235
	vir_da025_12119	388942205	388993333	40	0.4	49.8	55.4	216
HAMO-2 (VH2)	vir_da027_12167	393041401	393448174	90	11.7	39.4	62.9	745
	vir_da027_12172	393482194	393750738	70	5.1	43.4	64.9	757
	vir_da028_12176	393798660	394198821	85	9.2	42.5	44.9	671
	vir_da028_12181	394240935	394642154	100	12.1	33.7	73.7	750
	vir_da029_12186	394682113	395083339	100	11.4	38.6	39.4	676

	vir_da029_12191	395117073	395523035	90	10.9	35.6	39.8	695
	vir_da030_12196	395563239	395964285	100	8.9	33.3	27.2	660
	vir_da030_12201	396000361	396399590	50	1	60.3	70	674
Departure (RC4)	vir_da032_12238	399211375	399262951	26	26.5	68.3	65.7	6096

2.2 Calibrated VIR reflectance spectra

Creating global maps of Vesta with the VIR dataset require to mosaic 1,800 images acquired under various conditions of observations. Therefore, making seamless mosaics requires adjustment of the calibration for each detector. Calibration issues and corrections are presented in the following sections. In order to minimize systematic spectral and spatial artifacts, we developed a flat-field correction (section 2.2.1), and we calculated a new instrument response function (section 2.2.2). In addition, we normalized the data to a standard set of photometric conditions (section 2.2.4).

2.2.1 Flat-field correction

VIR radiance non-geographically projected images show vertical stripes when, with the spatial dimension of the slit on the horizontal axis. In this projection, each vertical line corresponds to the signal recorded by the same pixel. Vertical stripes appear when the pixel-to-pixel responsivity varies across one image displayed at a given wavelength. Assuming linearity of all the pixels (the number of electrons in output is proportional to the flux of photons received), relative pixel-to-pixel differences in responsivity can be corrected by one multiplier for each pixel. As a reference, we took the median responsivity of all pixels of a given wavelength λ for the entire VIR dataset at Vesta. The correction coefficient for pixel *i* is the ratio $\widetilde{Radiance(\lambda)}_{All\ Pixels} / \widetilde{Radiance(\lambda)}_{Pixel\ i}$, where $\widetilde{Radiance}$ is the radiance median value. This is performed independently for each wavelength of each detector. The resulting correction is a two-dimension file of coefficients (Fig. 2) that can be applied to each VIR dataset prior to performing data analysis. Fig. 3 illustrates the effects of the flat-field correction, which minimize the vertical striping in VIR observations, before geographic projection.

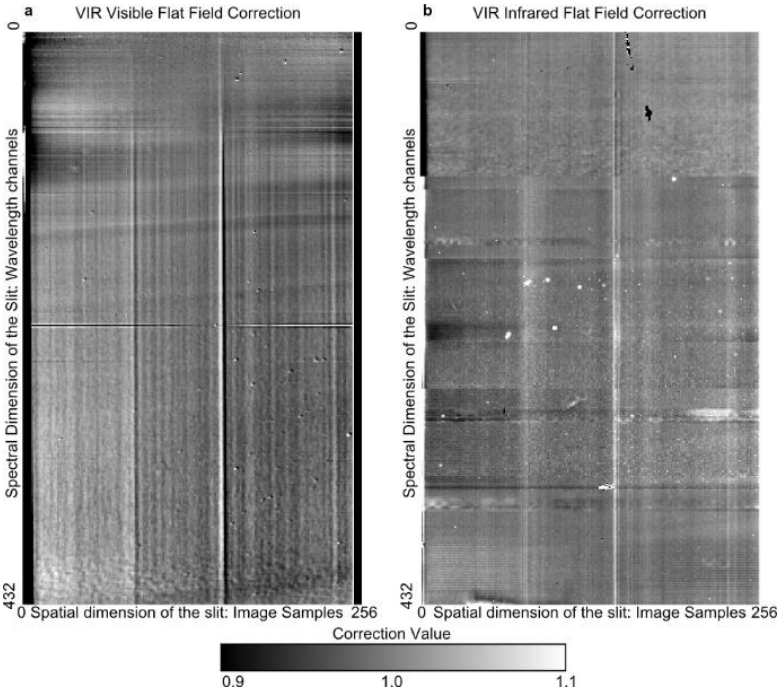

Fig. 2: Flat Field corrections for VIR Visible (a) and Infrared (b) detectors.

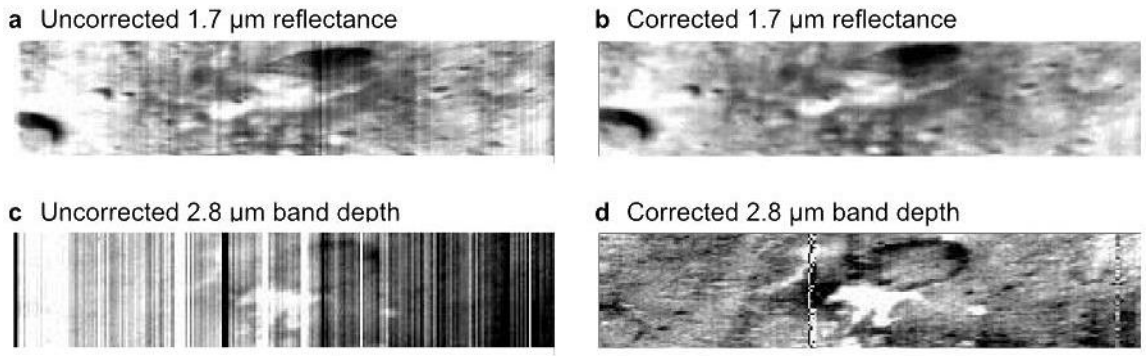

Fig. 3: Effects if incomplete calibration and correction of the flat-field on VIR IR observation 366905030 that covers Oppia crater and an adjacent surface unit rich in hydrated materials (bright pixels in 2.8 µm band depth images). a – Uncorrected 1.7 µm reflectance. b – Corrected 1.7 µm reflectance. c – Uncorrected 2.8 µm absorption band depth. a – Corrected 2.8 µm absorption band depth.

2.2.2 Instrument response function

After correction of the flat field, VIR spectra are normalized to the solar flux, from a model of solar spectrum, outside of the Earth's atmosphere (Thekaekara, 1973):

$$I/F = \frac{\pi I}{F_0 d^2},$$

where F_0 is the solar flux (irradiance) at 1 AU (Astronomical Unit), I is the calibrated radiance measured by VIR, and d is the distance from the surface of Vesta to the sun in AU.

VIR spectra show systematic high-frequency variations that appear in the average spectra of Vesta (Fig. 4 a and b). Furthermore, the infrared spectrum exhibits several peaks between 2.4 and 2.7 μm that are artifacts due to ground calibration errors. Residual amounts of water vapor in the vacuum calibration chamber introduced those peaks in the infrared responsivity function. In-flight calibration data performed with internal calibration lamps, confirmed the absence of spectral features in this range of wavelength, where a first new instrument response function was derived (step 1). Low signal-to-noise ration prevented the use of internal flight calibration data where one of those calibration error peaks occurred at 2.5 μm, therefore we completed the correction by manual removal of that peak alone and data interpolation to obtain a second function that we applied to the average spectrum of Vesta (step 2). Steps 1 and 2 are relevant to VIR IR only. Then we performed smoothing using a 5-channel wide boxcar average to the Vesta average spectrum for both VIR VIS (Fig. 4a) and VIR IR (Fig. 4b). The ratio between the corrected, smoothed spectrum and the raw spectrum constitutes the final response functions for VIR VIS (Fig. 4c) and VIR IR (Fig. 4d). We then processed the entire VIR dataset by applying those functions to each VIR spectrum. Note that no direct smoothing is performed to individual VIR spectra: only the average spectra are smoothed prior to computing new response functions. Finally, we performed a correction of high-frequency artifacts that occur systematically between odd and even channels by calculating the average of two contiguous channels (value computed between two channels), and then interpolating those average values at the wavelengths of the instrument. We have not observed measurable changes in the responsivity function over time, therefore we apply the same flat-field correction and instrument response function correction for the entire VIR dataset.

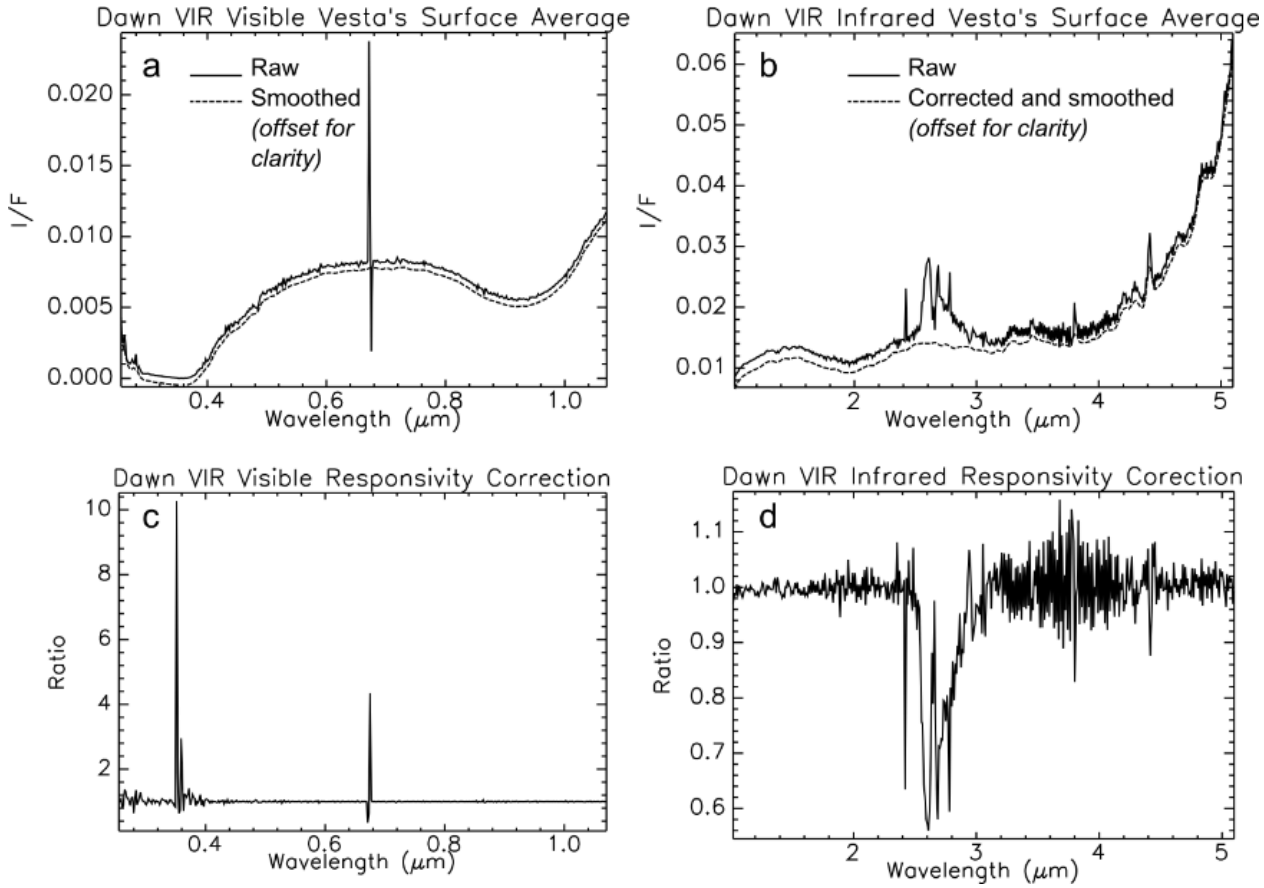

Fig. 4: VIR instrument response function correction. a – Visible I/F average spectrum of Vesta showing both raw and corrected spectra. b – Same as (a) in the infrared. c - Ratio of raw average visible spectrum of Vesta divided by the corrected spectrum. d – Same as (c) in the infrared.

2.2.3 VIR pointing information

Geometric information is computed through the standard the Navigation and Ancillary Information Facility (NAIF) SPICE system (Acton, 1996), assuming a detailed shape model of Vesta (Gaskell, personal communication to the Dawn team, 2013), using the latest attitude and trajectory files of the spacecraft reconstructed a posteriori from telemetry data, and following the International Astronomical Union (IAU) convention about longitudes for irregular bodies (increasing eastward in the range 0-360°). For each VIR pixel, the extension of the line of sight at infinity defines an intercept point and a local surface normal (SPICE sincpt function), which is used as a reference to compute the illumination angles (solar incidence and emergence) and the phase angle. Geographic coordinates, incidence, emergence and phase angles are needed for the mapping and photometric correction of VIR spectra. By the time the data were processed, the release of the N0065 Digital Shape model Kernel (DSK) from SPICE had a limited capability in handling irregular objects

defined by DSK shape models: Pieces of C/C++ computer codes accounting for shape models were implemented by NAIF for one SPICE function (named subpt_pl02.c). Thus we have implemented those pieces of codes for the aforementioned function (sincpt_c) that calculates the surface intercept of a ray from an observer to a target body, and the local surface normal.

In addition, we calculated geographic coordinates for each corner of each pixel, in order to project precisely the field of view corresponding to each VIR pixel. We calculated those sets of coordinates at the beginning and at the end of each observation by each pixel: This is the way to account for smearing that occurs during the integration time, due the relative motion of the spacecraft and the surface of Vesta, which makes the area observed by a given pixel (a cell) to move by several cell lengths.

The resulting pointing precision for both detectors is within the range of error that occurs between images acquired at different wavelengths.

2.2.4 Photometric correction

The last step in the calibration prior to making a mosaic is the correction of illumination effects due to the topography (disk-function) and surface scattering (phase function). Assuming the vestan regolith is generally similar to the lunar regolith, we chose a lunar model of the photometric correction that combines a disk function correction by Akimov (1975) and a phase function by Shkuratov et al. (1999). The Akimov function (equation 29 in Shkuratov et al. (1999) has no free parameter: it depends only on the incidence (i), emergence (e) and phase (a) angles. The Shkuratov function (equation 30 in Shkuratov et al. (1999) has four free-parameters: 1) the particle mean volume radius (d) divided by the wavelength of light under consideration (λ), 2) a parameter $k0$ sensitive to shadow-hiding effects, 3) the geometric albedo A, and 4) the length of the light-diffusion volume (L). We calculated all four free terms for each wavelength from VIR data of Vesta (we did not use the parameters calculated for the Moon). Fig. 5a shows the trend of VIR measurements as a function of phase after correction for the Akimov disk-function. To calculate the four free parameters, we computed a non-linear least squares fit of Eq. 1.

$$H(\alpha) = \frac{\exp(-k\alpha)}{2+exp\left(\frac{-d}{L}\right)}\left[2 + \frac{exp\left(\frac{-d}{L}\right)}{\sqrt{1+\left(\frac{4\pi L}{\lambda}\sin\frac{\alpha}{2}\right)^2}}\right] \qquad \text{Eq. 1}$$

where $k = k_0(1 - A)$ Eq. 2

We fed the partial derivatives of Eq. 1 with respect to the four parameters (Appendix) in a gradient-expansion algorithm. Iterations are performed until the chi square changes by a specified amount, or

248 until a maximum number of iterations have been performed. Fig. 5b illustrates the two-dimension
249 phase function modeled for all VIR wavelengths between 0.25 and 3.6 μm, and Fig. 6 shows the
250 four parameters as a function of wavelength. For the purpose of making seamless mosaics of
251 reflectance, we assumed the mean volume radius d and the Light-diffusion volume L are constant
252 across Vesta. The modeled bidirectional reflectance is first calculated with the global value A. Since
253 the albedo varies across Vesta, the modeled bidirectional reflectance at the geometry of illumination
254 and observation does not match the VIR dataset for a given pixel. Therefore, we performed iterative
255 adjustments for each VIR pixel of the geometric albedo A and shadow-hiding parameter k_0, which
256 are linked by Eq. 2. At each iteration, the global value of A is corrected by the factor (measured
257 reflectance/modeled reflectance). Iterations are performed until the difference between the modeled
258 and measured reflectance is less than 0.5%.
259 Spectra of the shadow-hiding parameter k_0 (Fig. 6b) and global geometric albedo A (Fig. 6c) vary
260 continuously across the entire range between 0.25 and 3.6 μm, and values agree between the visible
261 and infrared detectors of VIR. Larger amplitudes and high-frequency variations exist in spectra of
262 the mean volume scattering radius d/λ (Fig. 6a) and light-diffusion volume L (Fig. 6d). Although the
263 variations are not random, the spectra are noisy, and there are clearly three different regimes
264 between 0.25 and 0.9 μm (visible detector), between 1.1 and 2.7 μm, and between 2.7 and 5.1 μm.
265 The junction between the first two regimes around 1 μm is likely related to the instrument, as it
266 corresponds to the transition between the visible and infrared detectors. The third regime between
267 2.7 and 3.5 μm coincides with the occurrence of absorption bands of hydrated materials, and longer
268 wavelengths are affected by thermal emission of the surface. Since thermal emission is coupled with
269 surface temperature, it varies as function of the local incidence angle, time of day and topography.
270 Therefore, for wavelengths beyond 3.5 μm, variations of radiance as function of phase at a given
271 location on Vesta cannot be explained by the photometry alone: A model of thermal emission is also
272 needed. The regime of parameters d/λ and L between 2.7 and 3.5 μm shows similarity with the
273 thermal regime (beyond 3.5 μm), although it is not affected by thermal emission: This may indicate
274 variations of the absorption bands of hydrated materials as function of surface temperature and/or
275 solar illumination.
276 One consequence of the phase function correction is a modification of pyroxene absorption
277 band depths as function of the phase, consistent with results obtained by Longobardo et al. (2014).

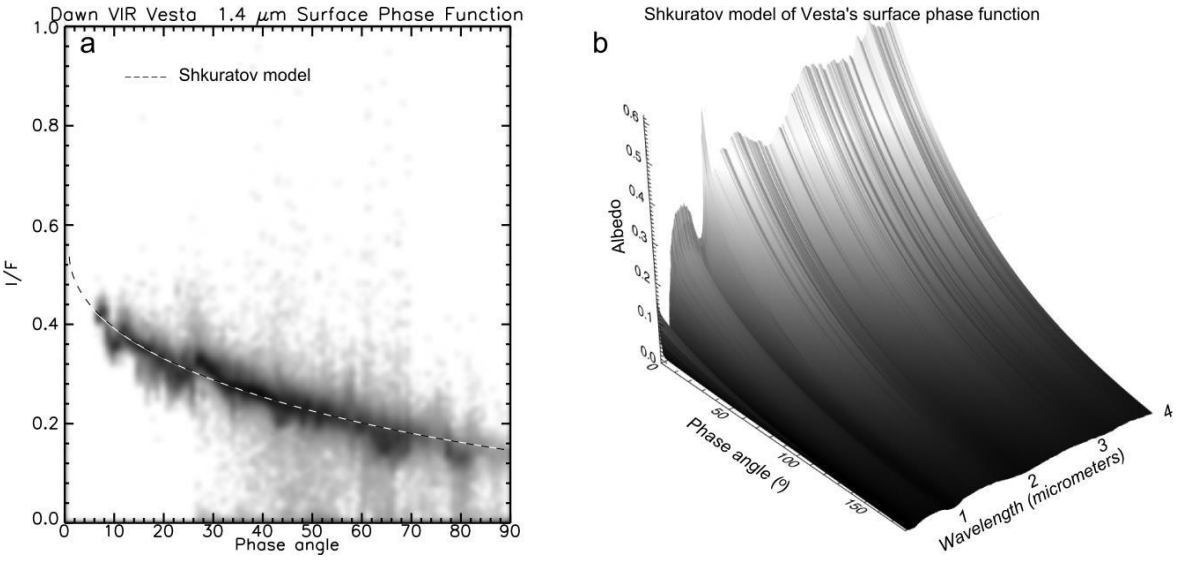

Fig. 5: a – Phase function at 1.4 μm of the entire surface of Vesta measured by VIR, after division by the Akimov disk function in order to minimize the illumination effects due to the topography. Darker pixels indicate a higher density of data. The dashed line is the Shkuratov model. b – Modeled Shkuratov phase function for the entire surface of Vesta and for all VIR wavelengths between 0.25 and 3.8 μm.

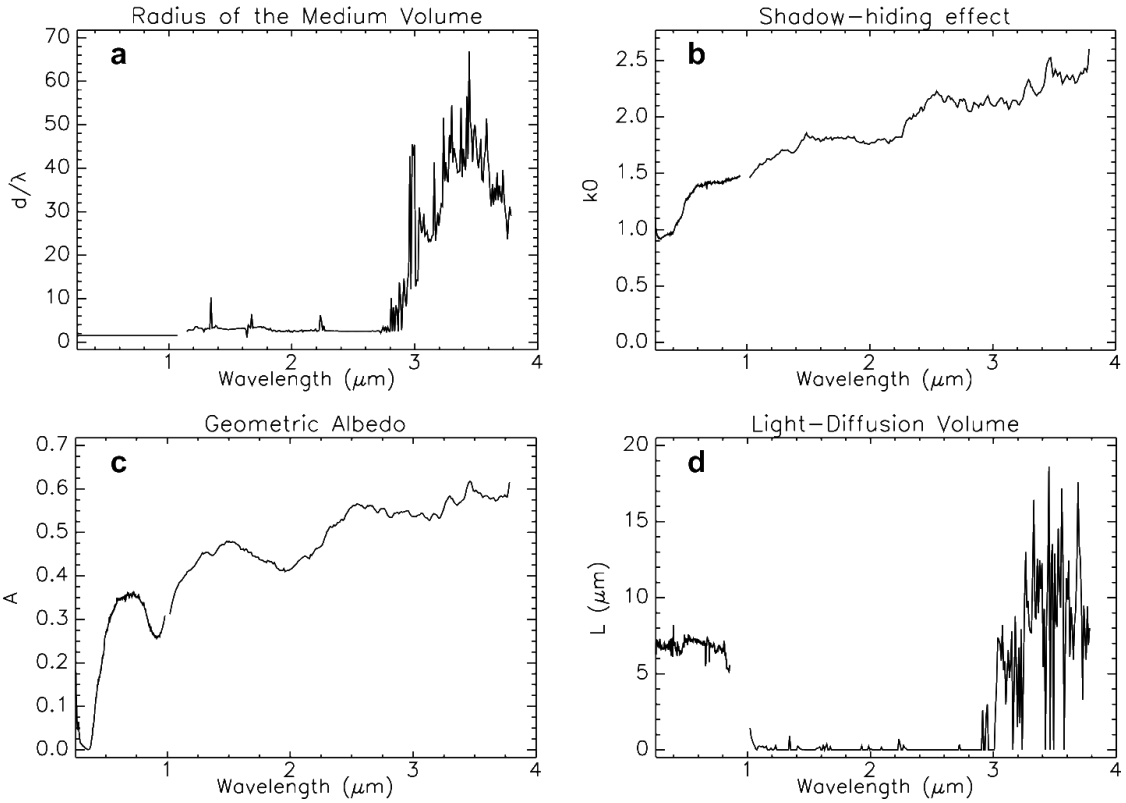

Fig. 6: Shkuratov phase function modeled parameters for the surface of Vesta, as observed by VIR. See text for explanation of significance of (a) Radius of the Medium Volume, (b) Shadow-hiding parameter, (c) Geometric Albedo and (d) Light-Diffusion Volume parameter.

We chose this method because it relies on a phase function based on physical properties of the regolith (Shkuratov et al., 1999), and the capability of calculating all phase function parameters with a semi-analytical, partial derivative inversion technique. From our experience, this approach is faster and produces fewer non-unique solutions than non-analytical inversions. The fact that we achieved seamless mosaicking and mapping Vesta with VIR data (Fig. 7) is a quality criterion that can be valued for future use of this model for more detailed interpretation of the Shkuratov photometric parameters. The two steps of the photometric correction are illustrated by VIR IR spectra in Fig. 8, Spectra of the same area observed three times (364433539 and 364435639 during Approach and 371683119 during HAMO) under different geometries of illumination and observation (Fig. 8a) are shown in Fig. 8b in I/F (no photometric correction applied). If the surface was a perfect scatterer, all three spectra should superimpose each other; differences between the spectra are due to the photometry. Applying the Akimov disk-function (Fig. 8c) leaves remaining effects of the phase angle which, in this example of apparent reflectance, introduces larger differences than between I/F spectra. Phase angle effects are corrected in (Fig. 8d) by the Shkuratov function, which make the three reflectance spectra match with a ~0.01 error between 1.0 and 2.5 μm. The two spectra from Approach also match between 2.5 and 3.5 μm once calibrated into reflectance, however the spectrum from HAMO has lower reflectance by 0.03. This may indicate a temporal variation in the absorption bands of hydrated materials. This is consistent with the differences of the photometric regimes illustrated in Fig. 6a and Fig. 6d. When the intrinsic spectra shape varies as function of time, either due fluctuations of abundance or physical properties, the photometric correction is not enough to retrieve the absolute reflectance.

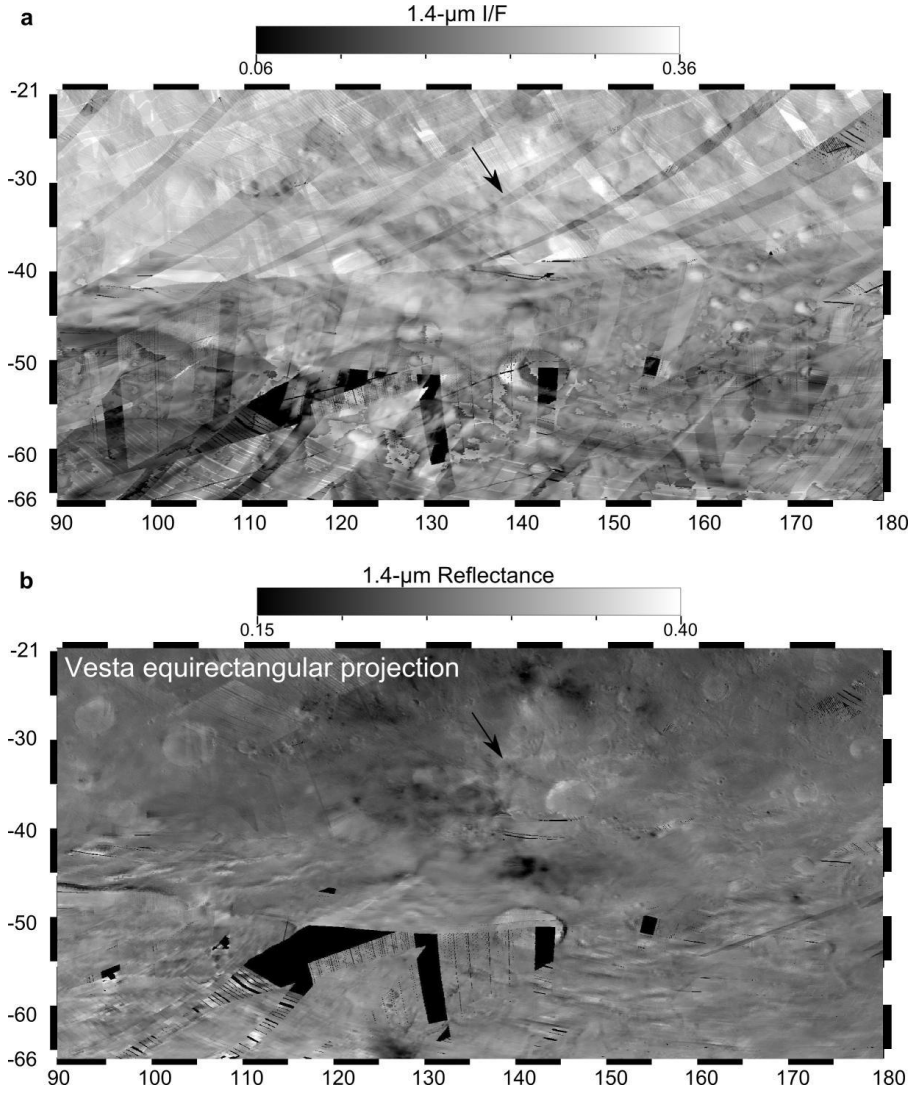

Fig. 7: Reflectance normalization by photometric correction of VIR data of Vesta minimizes seams between images projected in a mosaic. Example of the Sextilia quadrangle on at 1.4 μm. The black arrow indicate the location where spectra of Fig. 8 have been collected. a – I/F, before photometric correction. b – Reflectance, after correction of the Akimov disk-function and the Shkuratov phase function.

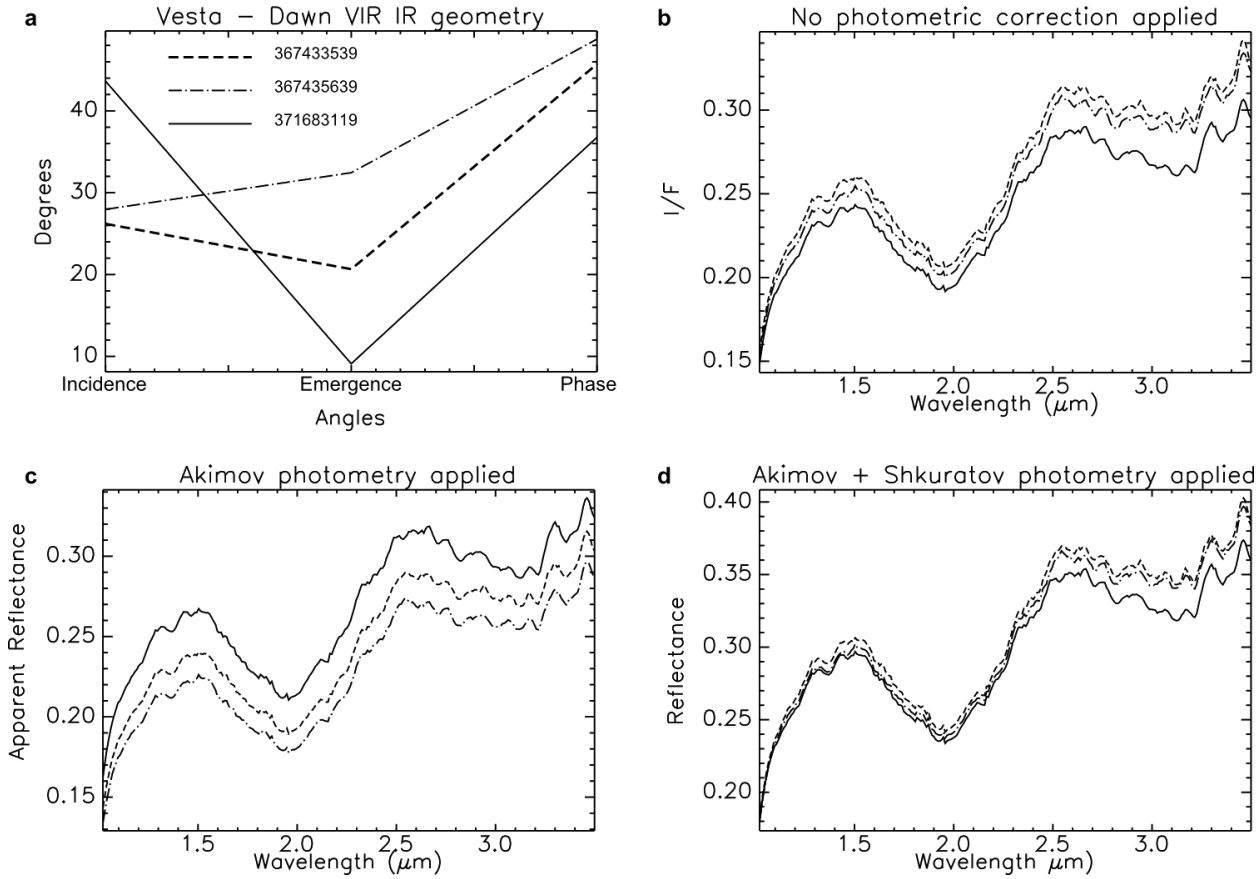

Fig. 8: Example of the effects of the photometric correction on three VIR IR spectra of a ~500 × 500 m area at 32° 48' 40.54" S and 138° 36' 23.75"E (location indicated as a black arrow in Fig. 7) acquired at different times and under different geometries of illumination and observation. a – Incidence, emergence and phase angles for the three observations. b – The radiance factor I/F is defined as radiance divided by the solar irradiance, without any photometric correction applied. c – The apparent reflectance is I/F corrected for the photometric effects of the topography according to the Akimov disk function. d – The bidirectional reflectance includes the Shkuratov phase function and normalization at 30° incidence and 0° emergence.

2.3 2.8-μm absorption band depth

Mapping of the absorption band depth of hydroxyl relies on the calculation of a difference between a linear continuum anchored at the two shoulders of the band (in the range 2.6476 - 2.6668 μm and 2.9031 - 2.9222 μm respectively) and the reflectance at the center (average in the range 2.7895 - 2.8087 μm). The technique illustrated in Fig. 9 is the same as presented in De Sanctis et al. (2012).

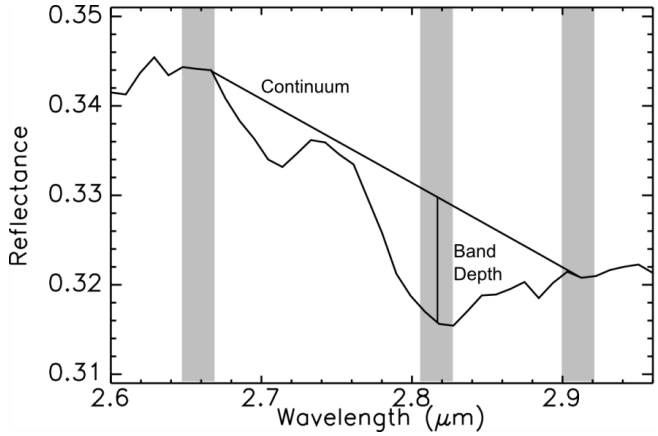

Fig. 9: Illustration of how the 2.8 μm absorption band depth of hydrated materials is measured froim VIR spectra of the surface of Vesta. A straightline continuum is defined between the shoulders of the band. The badn depth is calculated between the continuum and the spectrum.

2.4 Geographic projection

In order to optimize the signal-to-noise ratio of the maps, we integrated the entire VIR dataset from Approach, Survey, HAMO-1 and HAMO-2, and we projected the data on a global geographic grid. The side of each cell of the grid is approximately 200 m. To cover all the longitudes from meridian to meridian at the equator 8325 cells are needed, while one cell covers the North and South poles. This technique does not oversample the high latitudes, which is the case for an equirectangular projection. This is appropriate because Dawn's orbit was not polar, and the coverage was relatively even as function of latitude, except for the northern regions. The grid is an intermediate step which enables faster computation of maps in any projection. Equirectangular maps and polar maps constitute the final product presented in other papers in this Vesta Surface Composition special issue.

The geographic coordinates used in all the maps refer to the Claudia System, which was established by the Dawn Team with prime meridian near the center of Claudia crater (1.6°S and 356.0°E). This system positions the quadrangle maps so that their borders do not bisect any major surface features. An alternate system known as the International Astronomical Union (IAU) Coordinate System for (4) Vesta (also named Claudia Double Prime System) is defined by assigning a positive longitude of 146° to Claudia.

In order to display a complete VIR spectrum that includes data from both visible and infrared detectors, all the calibration and geographic projection steps described in sections 2.2 and 2.4 are necessary. In the range of wavelengths where the two detectors overlap (1.02-1.07 μm), VIR VIS data are removed. No additional correction is performed.

3. Results: Global maps and statistics for all quadrangles

Final global maps in the equirectangular projection of the 1.4 μm reflectance (Fig. 10) and the 2.8 μm band depth (Fig. 11) cover more than 92% of the surface of Vesta, except for a few gaps in the southern hemisphere and with very little coverage northern of 60°N. The two maps show units that are spatially coherent, which indicates the observed variations are likely due to the surface material composition. Another criterion of quality is the absence of seams in the mosaics, which means the boundaries between individual VIR observations are not visible, as it should be. In particular there is no obvious effects related to incidence or phase angles. Instead, most variations correspond to morphological features, such as impact craters and their ejecta, or spectral properties related to pyroxene absorption bands (Frigeri et al., 2015, this issue).

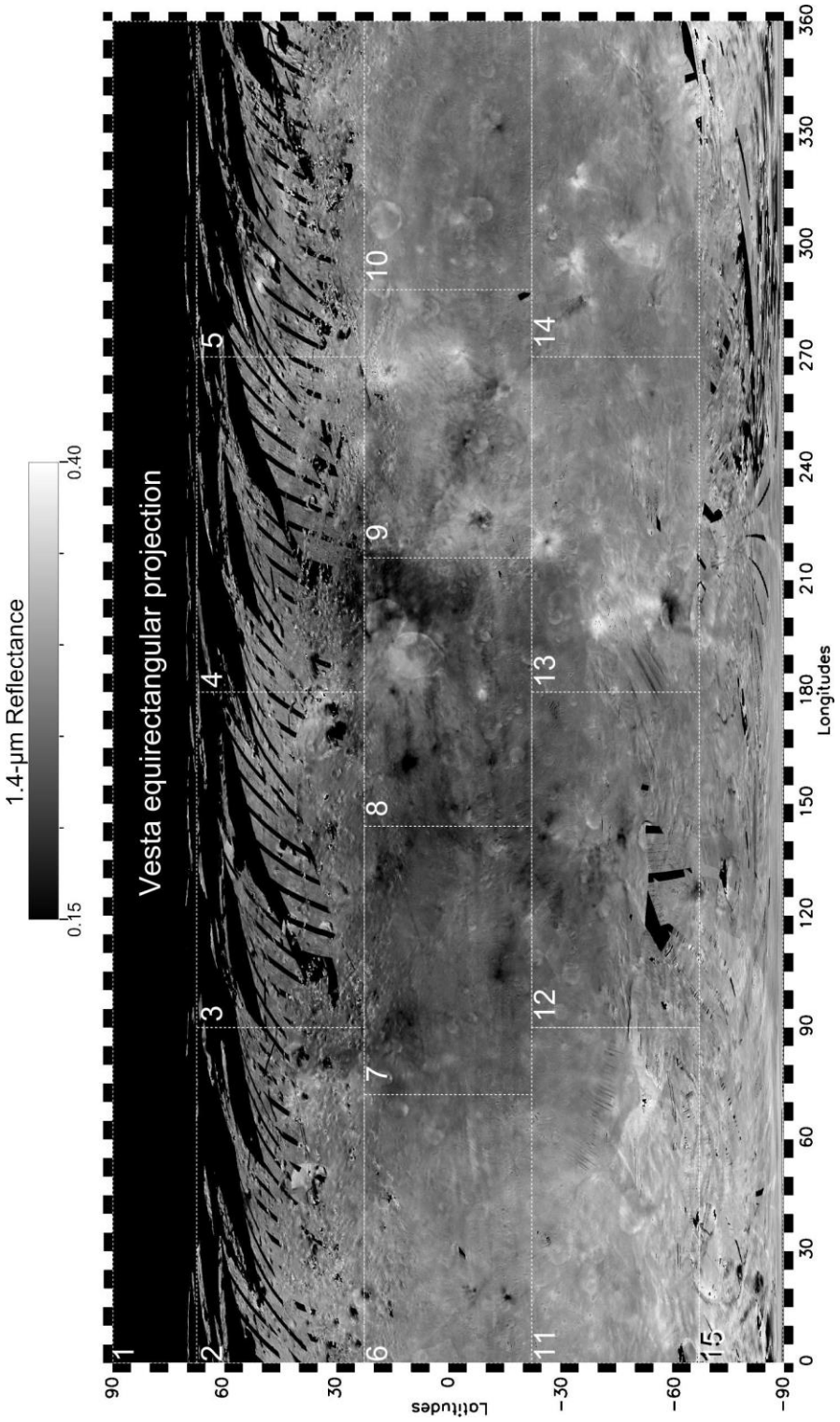

Fig. 10: Vesta's surface global map of reflectance at 1.4 µm, observed by VIR after photometric correction. The dashed-line rectangles correspond to the conventional division into fifteen quadrangles (Williams et al., 2014), numbered and named as follows: 1) Albana, 2) Bellicia, 3) Caparronia, 4) Domitia, 5) Floronia, 6) Gegania, 7) Lucaria, 8) Marcia, 9) Numisia, 10) Oppia, 11) Pinaria, 12) Sextilia, 13) Tuccia, 14) Urbinia and 15) Rheasilvia.

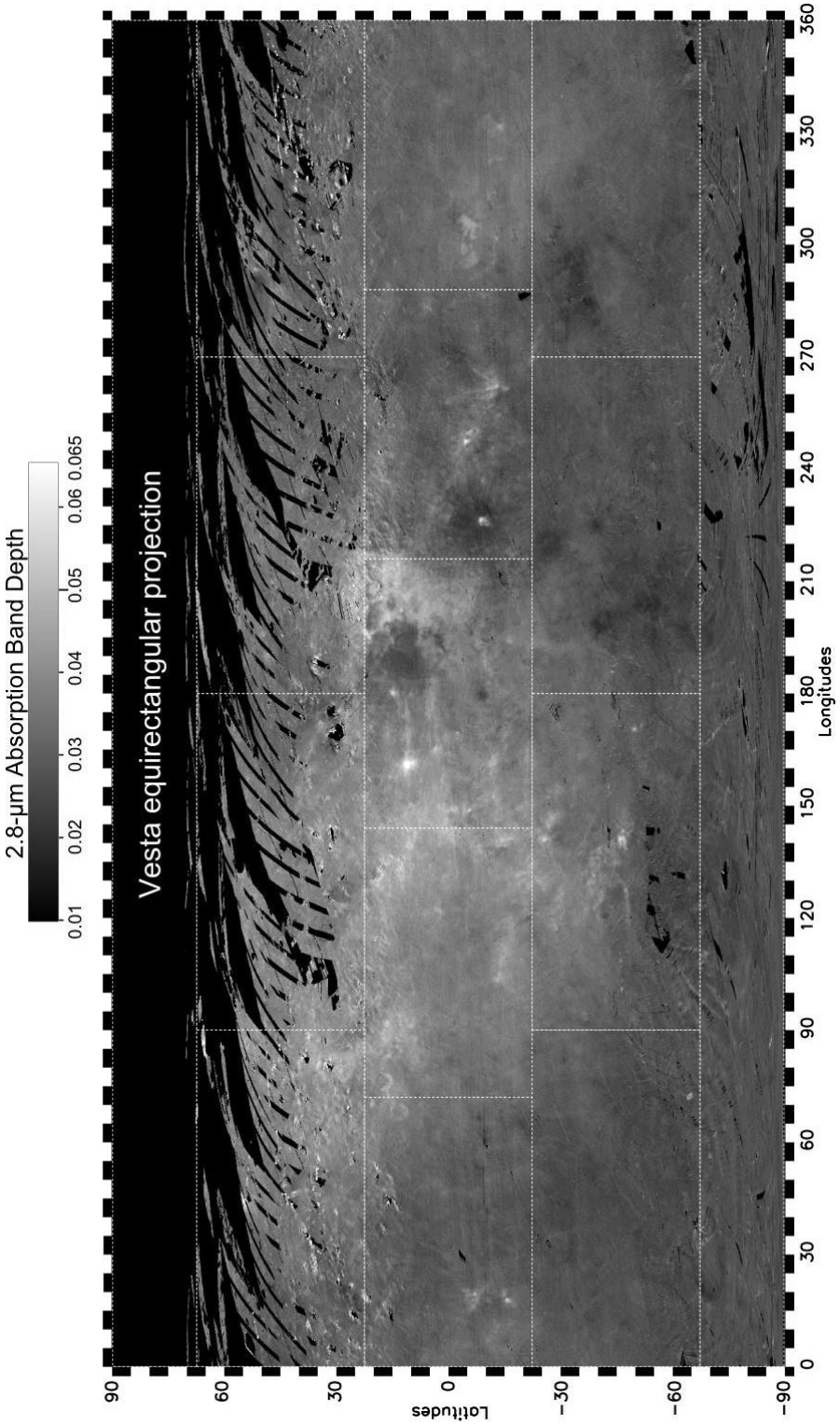

Fig. 11: Vesta's surface global map of absorption band depth of hydroxyl at 2.8 µm. The dashed-line rectangles correspond to the conventional division into fifteen quadrangles.

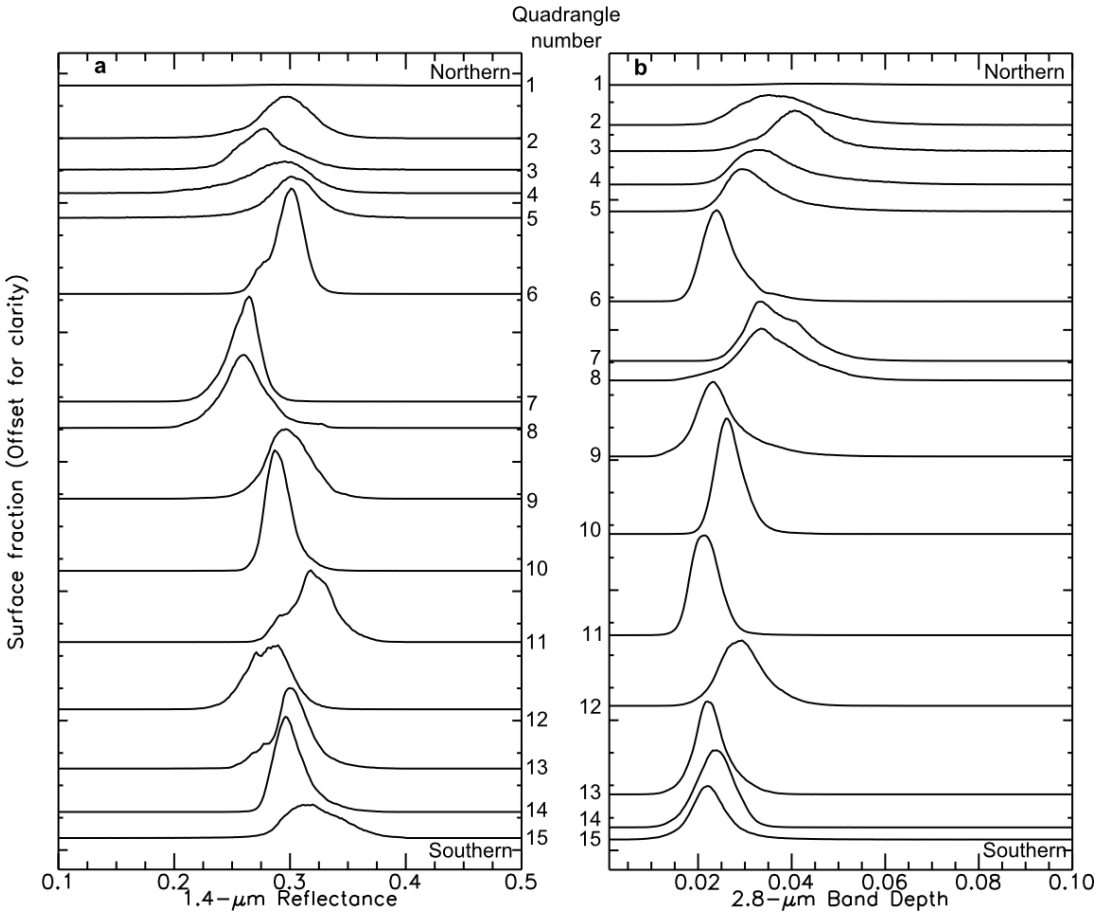

Fig. 12: Vesta's surface histograms calculated from VIR observations for all fifteen quadrangles, numbered between the two panels from the north pole on top to the south pole at the bottom. a – 1.4 μm reflectance. b – 2.8 μm absorption band depth of hydroxyl.

Fig. 12 breaks out the statistics of reflectance properties (1.4 μm reflectance and 2.8 μm absorption band depth) for the fifteen standard quadrangles defined by the Dawn team (Roatsch et al., 2012). The histograms indicate generally unimodal distributions, showing that both albedo and hydrated material vary smoothly across Vesta, and large dark hydrated areas do not have sharp boundaries. In the histogram curves, multiple inflections and asymmetry may exist, which indicate that small compositional units within a given quadrangle may differ from the surrounding areas and may have sharp boundaries. Although the shape and position of pixel distributions of albedo and hydrated materials are anti-correlated in general, differences exist (quadrangles 6, 7, 11, 12 and 13 are examples), where unusual regions contain hydrated and relatively bright materials, or relatively dark and little to no hydrated materials. According to stacked histograms in Fig. 12, dark hydrated materials are the most frequent in the northern hemisphere. Within a given interval of latitudes, the northern regions above 22°N and equatorial latitudes between 22°S and 22°N have the largest

386 diversity and as function of longitude, because of the largest areas of hydrated dark materials
387 between 90°E and 210°E.

388 4. Discussion: Spectral properties and distribution of dark and hydrated
389 materials

390 4.1 General distribution characteristics of dark and hydrated materials on Vesta

391 To first order, the 1.4 μm reflectance (Fig. 10) and 2.8 μm absorption band depth (Fig. 11) are anti-
392 correlated, and visual inspection of the two maps is not sufficient to determine whether some
393 surface units depart from this trend and characterize different processes. The color map of 1.4 μm
394 reflectance vs. 2.8 μm band depth (Fig. 13**Error! Reference source not found.**) illustrates the
395 broad-scale distribution of dark, hydrated materials, as well as more rare surface units that do not
396 show obvious correlations between the two parameters. Saturated colors correspond to the
397 periphery of the data cloud in the 2-D scatter plot as a way to locate the endmember compositions.
398 The center of the cloud, where the highest density of points occurs, translates into darker pixels on
399 the map. If Vesta's materials were all on a well-defined trend of dark hydrated and bright little to no
400 hydrated components, orange, blue, and black would be the only colors on the map. A broad region
401 of Vesta, between 30°S and 30°N, and 90°E and 210°E contains dark (Reddy et al., 2012, McCord
402 et al., 2012; Li et al., 2013), hydrated (De Sanctis et al., 2012; McCord et al., 2012), hydrogen-rich
403 (Prettyman et al., 2012) and eucritic compositions (McCord et al., 2012; Reddy et al., 2012;
404 Prettyman et al., 2012; McSween et al., 2013; Ammannito et al., 2013a), which is consistent with the
405 analysis of dark material units at small scale (Palomba et al., 2014) as well as with photometric
406 analysis (Schröder et al., 2014). Generally, diogenitic surfaces have low amounts of hydroxyl (De
407 Sanctis et al., 2013). The trend between dark hydrated (blue pixels) and bright, non-hydrated
408 materials (orange pixels) represents most of the surface of Vesta. Other regions (the minority) do
409 not follow this trend. Green pixels indicate areas with relatively high albedo and deep 2.8 μm band:
410 they define spatially coherent regions, mostly in the northern hemisphere, roughly defined by the
411 Bellicia, Arruntia and Pomponia craters, where different mafic composition may correspond to
412 olivine (Ammannito et al., 2013 b), between Caesaria and Capparonia craters which absorption
413 bands of mafic minerals are more similar to the average of Vesta (Ammanito et al., 2013a, Frigeri et
414 al., 2005, this issue), and the ejecta blanket western of Oppia (Tosi et al., 2015, this issue), which has
415 a broad and asymmetric absorption band between 2.8 and 3.5 μm that is different from most areas

on Vesta. Red and magenta pixels, characteristic of relatively dark and little to no hydrated materials, occur mostly in the southern hemisphere, between Severina and Lucilla craters, between Antonia and Herennia craters, and between Urbinia and Sossia craters (Zambon et al., 2015, this issue).

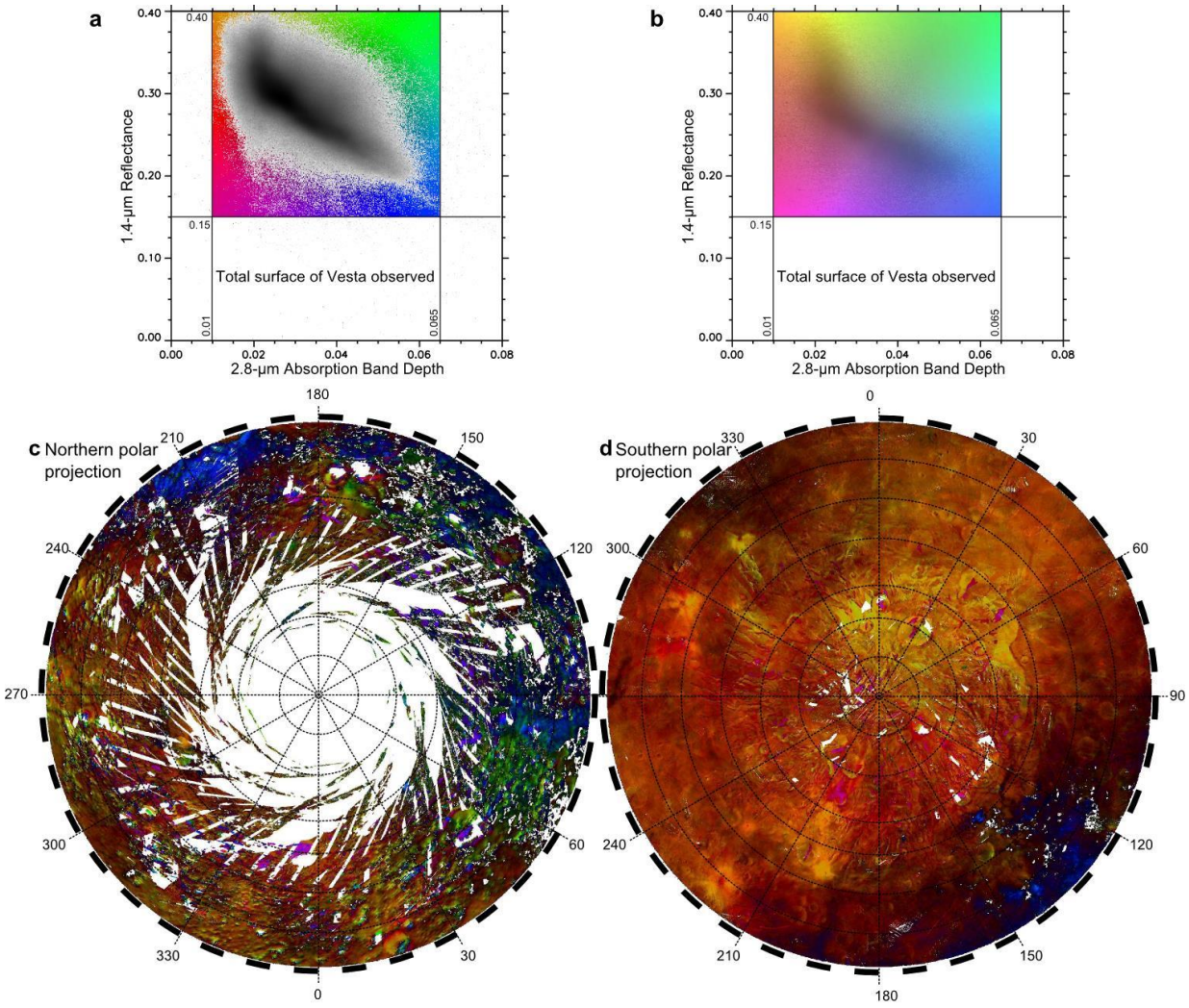

Fig. 13: a – Two-dimension scatter-plot of the total surface of Vesta observed by VIR for the reflectance at 1.4 µm as function of the 2.8-µm absorption band depth of hydroxyl. The color scheme is designed to enhance the location and boundaries of the data cloud. b – Same as (a), except the colors represented have a direct correspondence to the colors on the map. c, d and e – Color composite of 1.4 µm reflectance vs. 2.8 µm band depth, as defined by the color scale on top (b) for the northern regions above 22°N (c), the southern regions below 22°S (d), and the entire surface of Vesta in equirectangular projection €. Regions in green pixels indicate areas with relatively high albedo and deep 2.8 µm band. They define a spatially-coherent region including Bellicia, Arruntia and Pomponia craters, as well as a smaller region near Oppia. The dashed-line rectangles correspond to the conventional division into fifteen quadrangles.

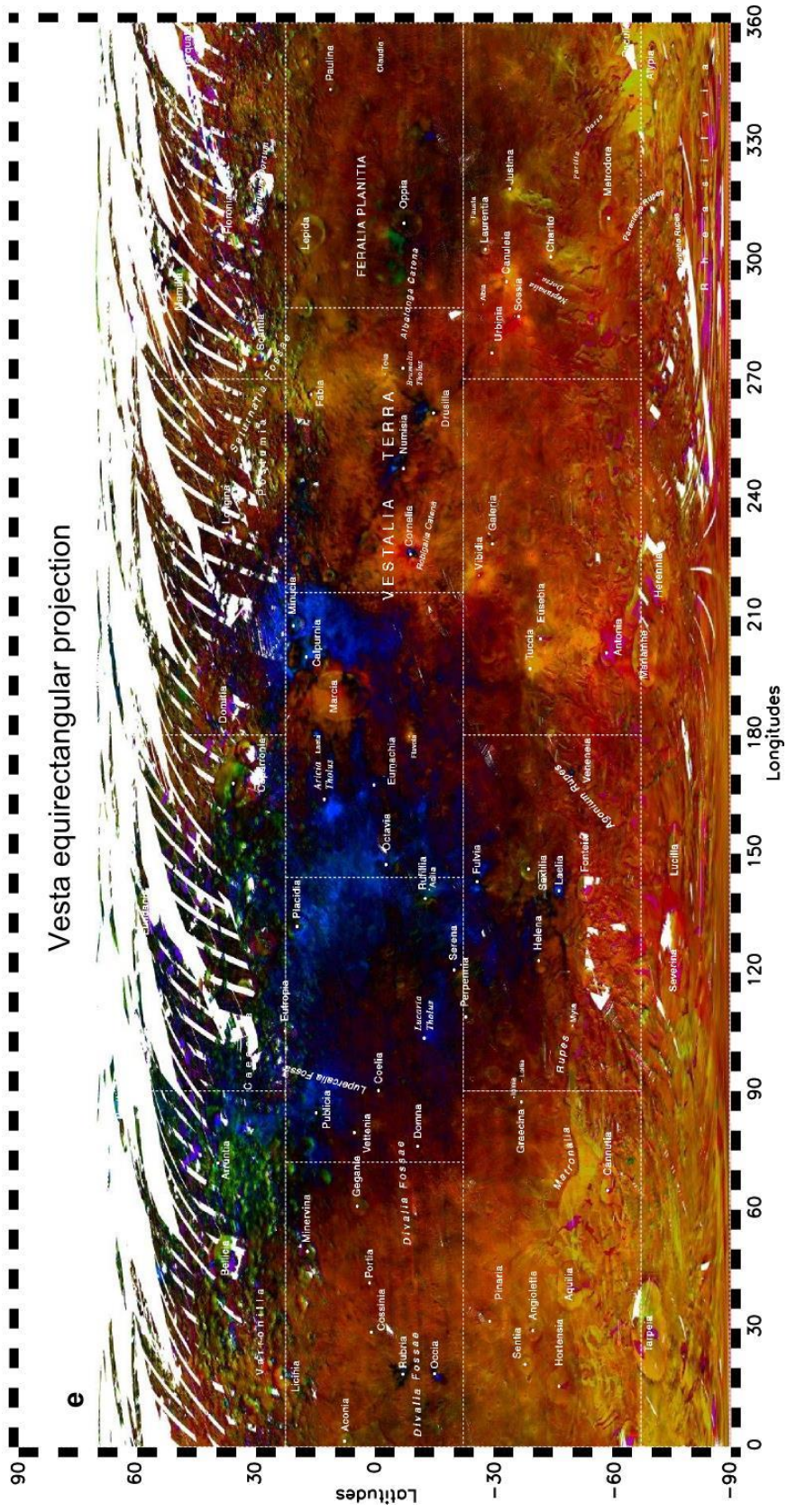

Fig. 13 (continued).

4.2 Investigation of the origin of dark materials using spectral slope

In order to evaluate spectral properties associated with dark hydrated materials, we carried out further analysis of VIR spectra. Linear spectral unmixing performed by McCord et al. (2012) between 1.0 and 2.5 μm revealed that dark materials on Vesta have weaker pyroxene absorption bands and a more positive spectral slope than higher-albedo surface units. As a test, and in order to illustrate these properties at global scale, we normalized all VIR spectra at 1.4 μm, and we calculated the average spectral slope (Fig. 14) by fitting a straight line between 0.4 and 2.5 μm.

At first order, the infrared spectral slope is correlated with dark materials. This is supported by Cloutis et al. (2013), stating that Mighei-type carbonaceous chondrite (CM2) material may cause an optical reddening (more positive spectral slope).

Variations of average spectral slope in the visible and near-infrared (Fig. 14) differ from the ratio in the visible $R_{0.75\ \mu m}/R_{0.44\ \mu m}$ (e.g. Reddy et al., 2012; Le Corre et al., 2013) with FC data. In the visible, ejecta of Oppia and Octavia craters have a more positive spectral slope than dark materials. The visible ratio is sensitive to a spectral slope and to an intense metal-O charge transfer absorption (Wagner et al., 1987; Cloutis et al., 2008) which is the deepest between 0.30 and 0.35 μm. This UV absorption exists in all pyroxenes, olivines and carbonaceous chondrites and is likely saturated (Fig. 4a), which explains why maps of spectral slopes in the visible and infrared do not look similar. According to Le Corre et al. (2013), observation of a spectral reddening in both FC and VIR data indicates the possibility of impact melt composition in some surface units. This interpretation is supported by analysis of the morphology, which may indicate impact melt flows on the surface (Williams et al. 2014). Reddy et al (2012a) show that the albedo of impact melt is not as low as if it was due to the contamination by carbonaceous chondritic material. Impact melt may not have an intrinsically stronger absorption band in the UV, however, there is a relationship between the efficiency of absorption processes and particle sizes (e.g. Hapke, 1993). Surface materials with impact melt contains small dispersed vitrified particles which may favor a stronger and broader absorption process in the UV that appear in the visible ratio $R_{0.75\ \mu m}/R_{0.44\ \mu m}$.

4.3 Relationship of dark materials with pyroxene absorption band depth

In order to evaluate the contrast of the pyroxene absorption bands independently from the albedo and spectral slope, we divided each spectrum by its own spectral slope. Then we calculated the standard deviation, which measures variations of reflectance in the range 0.4-2.5 μm for each spectrum. In Fig. 15, higher values for the standard deviation indicate stronger pyroxene absorption

463 bands. Our results confirm that, to first order, Vesta's dark materials have a more positive spectral
464 slope and weaker pyroxene absorption bands. As a corollary, bright materials have stronger
465 pyroxene absorption bands and contain all types of HED compositions (Zambon et al., 2014).
466

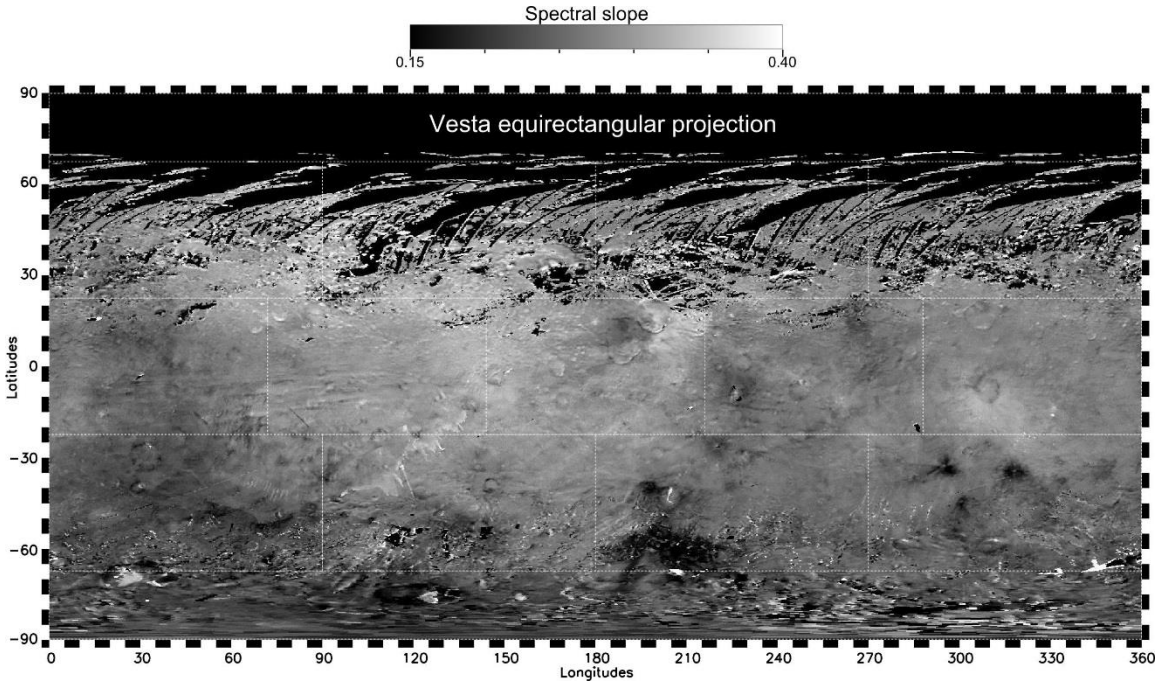

467
468 **Fig. 14: Vesta global distribution of spectral slope from VIR reflectance data between 0.4 and 2.5 μm, after**
469 **normalization at 1.4 μm. The dashed-line rectangles correspond to the conventional division into fifteen**
470 **quadrangles.**

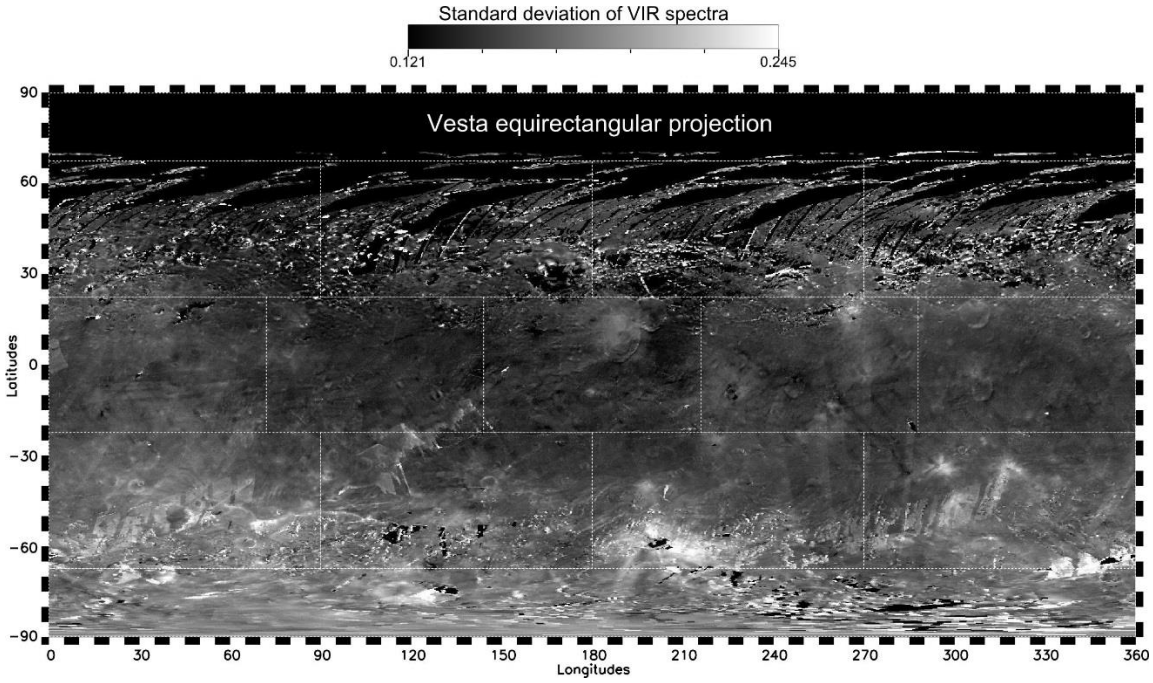

Fig. 15: Vesta global distribution of standard deviation of VIR reflectance data between 0.4 and 2.5 μm, after normalization at 1.4 μm. This parameter is sensitive to the depth of the two pyroxene absorption bands. The dashed-line rectangles correspond to the conventional division into fifteen quadrangles.

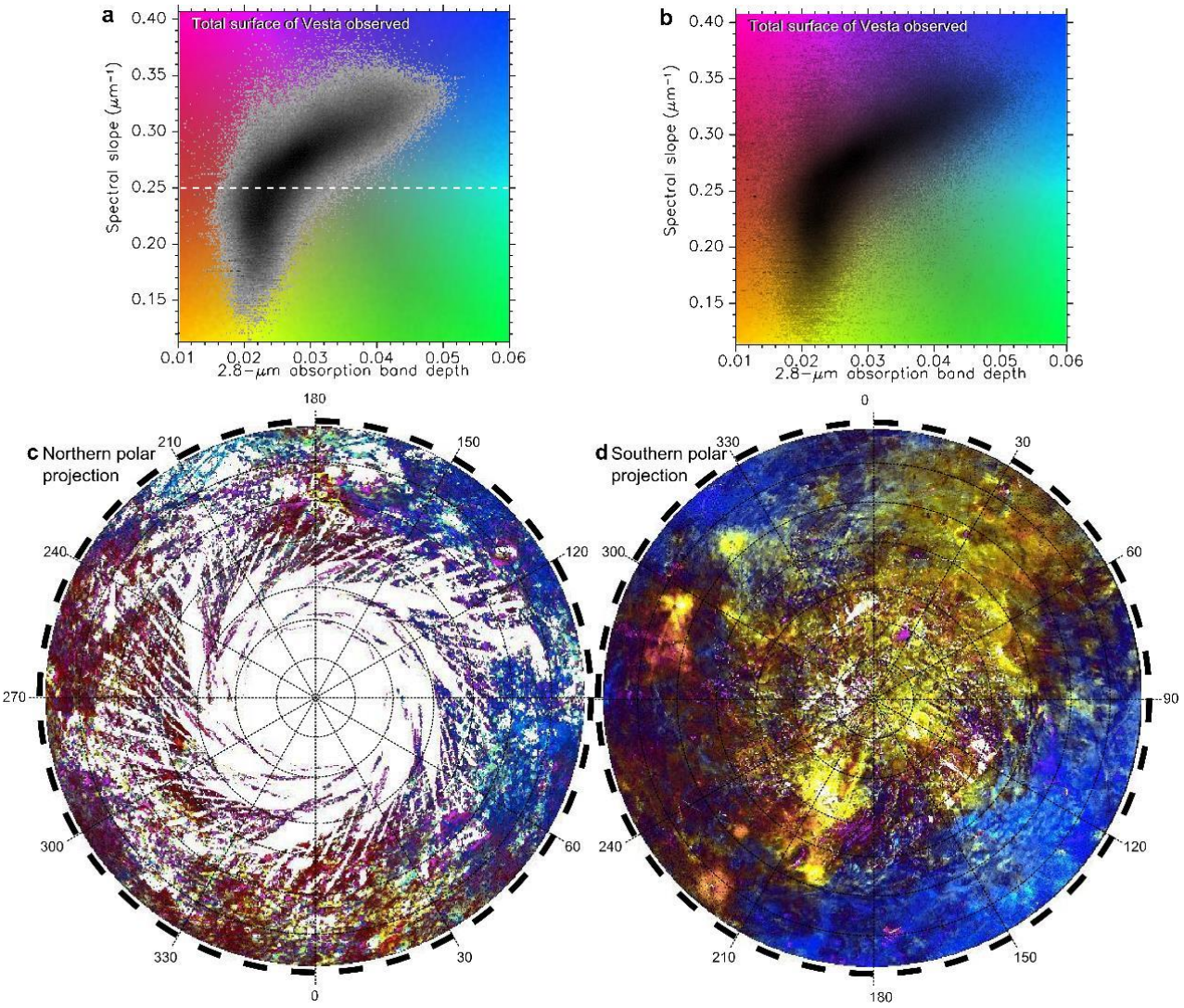

Fig. 16: a – Two-dimension scatter-plot of the total surface of Vesta observed by VIR for the spectral slope as a function of the 2.8 μm absorption band depth of hydroxyl. The color scheme is designed to enhance the location and boundaries of the data cloud. b – Same as (a), except the colors represented have a direct correspondence to the colors on the map. c, d and e – Color composite of spectral slope vs. 2.8 μm band depth, as defined by the color scale on top (b) for the northern regions above 22°N (c), the southern regions below 22°S (d), and the entire surface of Vesta in equirectangular projection €. The dashed-line rectangles correspond to the conventional division into fifteen quadrangles.

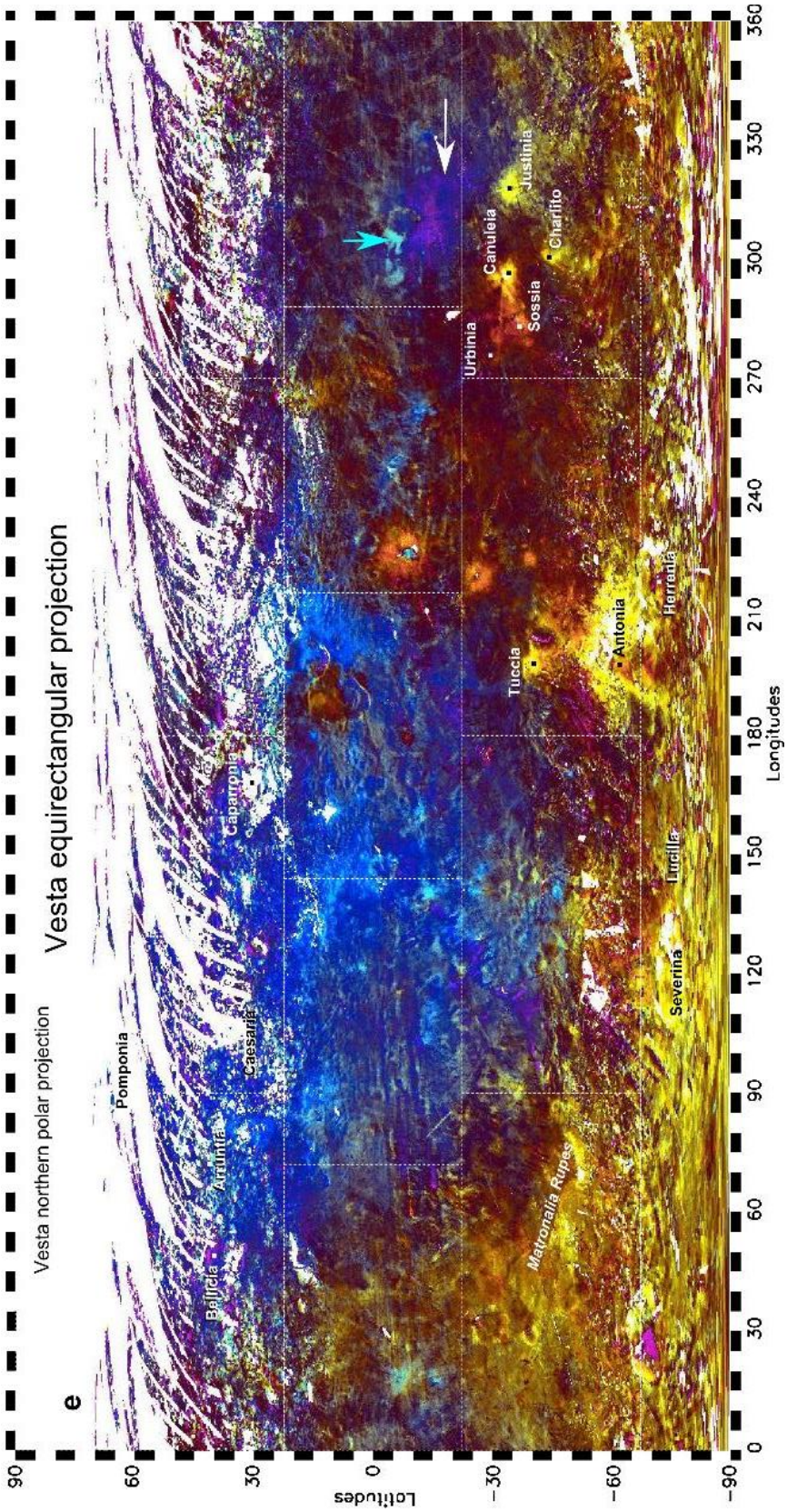

Fig. 16 (continued).

485 **4.4 Relationship of dark, hydrated materials and spectral slope**

486 The color map of spectral slope vs. 2.8 μm band depth (Fig. 16) shows two diffuse linear trends.
487 This dual behavior is likely a real characteristic of Vesta's surface materials, since variations across
488 the surface of Vesta of the spectral slope and 2.8 μm band depth define spatially coherent units, and
489 multiple observations of the same areas have been used to make the maps. Similar to Fig. 13,
490 saturated colors correspond to the least frequent compositions on Vesta, which are also likely the
491 most pure that can be observed.

492 *4.4.1 Terrains with little to no hydrated materials*

493 The left side of the plot in Fig. 16a where the background is yellow, orange or red, below the
494 dashed line, corresponds to weak 2.8 μm band depth. The shape of the data cloud elongated
495 vertically indicate spectral slope variations exist without significant change of the 2.8 μm band depth
496 On the maps, these colors occur mostly in the southern hemisphere. In yellow, a weak hydroxyl
497 absorption band associated with a moderate spectral slope occurs in Rheasilvia basin, including
498 Matronalia Rupes and Severina craters, Antonia crater and its ejecta, and on more localized areas
499 near Tuccia, Canuleia, Justinia and Charlito craters. Note that the entire region identified as
500 Rheasilvia ejecta (Combe et al., 2015 this issue; Longobardo et al., 2015 this issue) has similar
501 characteristics, only slightly subdued with respect to the freshest craters, as indicated by unsaturated
502 colors. One exception is Teia crater in the northern hemisphere, north of Vestalia Terra. The
503 distinction between Rheasilvia type of material (basin and ejecta) and the rest of Vesta appears more
504 obviously in this representation than in Fig. 13. In particular, the entire region south of Vestalia
505 Terra (Buczkowski et al., 2014) – which includes Numisia quadrangle and the northern and western
506 parts of the Antonia quadrangle – has dark red pixels in Fig. 16, indicating of a more positive
507 spectral slope occurring for terrains with little to no hydrated materials.

508 Other types of compositions rarely found on Vesta combine weak 2.8 μm absorption band and
509 weak spectral slope, such as units found around Vibidia, Cornelia, Urbinia and Sossia craters.
510 Steeper spectral slopes sometimes occur in ejecta of relatively fresh craters. Wherever a strong
511 positive spectra slope is observed without a significant absorption by hydrated materials, the surface
512 is unlikely to contain much carbonaceous chondritic particles. Ejecta likely consist of rougher
513 terrain and larger particle sizes than surrounding areas. Because both roughness and grain size have
514 dimensions smaller than a pixel size, the characterization of their scattering effect can only be done
515 statistically, which is typically accounted by photometric models (e.g. Hapke, 1981; Shkuratov et al.,

516 1999). Therefore, in order to establish a link between steeper spectral slopes and physical properties
517 of the surface, further investigations shall be performed by means of photometric modeling.

518 *4.4.2 Terrains with variations of hydrated materials*

519 Materials that are characterized by a spectral slope higher than 0.25 μm^{-1} (upper part of the two-
520 dimension scatter plot in Fig. 16a, above the dashed line) show a positive correlation of spectral
521 slope with the 2.8 μm band depth. Corresponding colors (Fig. 16b) include a blue component, such
522 as magenta, purple, cyan and pure blue. The broad equatorial region in blue between 90°E and
523 180°E is the typical dark hydrated materials (carbonaceous chondritic). The northern regions above
524 50°N contain a few areas in purple, such as Capparonia, which is peculiar because it is relatively
525 bright while hydrated (green pixels in Fig. 13). The most striking occurrence of a very positive
526 spectral slope on hydrated materials is located in a surface unit south of Oppia represented in deep
527 blue (pointed by an oblique, white arrow in Fig. 16), mapped as an orange/red area by Reddy et al.
528 (2012b) and Le Corre et al. (2013) in a ratio color composite from the Framing Camera suggesting
529 impact melts (Le Corre et al., 2013) and contamination by carbonaceous chondritic material (Tosi et
530 al., 2015, this issue). The ejecta blanket western of Oppia (cyan area pointed by a vertical arrow in
531 Fig. 16) is also different from the rest of Vesta, as it shows hydrated materials and a moderate
532 spectral slope, associated to relatively high albedo. This area with lobate boundaries corresponds to
533 light orange/pumpkin patches seen in ratio color composite from the Framing Camera (Le Corre et
534 al., 2013). Tosi et al. (2015, this issue) provides a detailed description and discussion about the
535 finding of a correlation between spectral signature of hydrated materials and light orange patches.
536 The Rufillia and Rubria craters have also moderately positive spectral slope and high strong hydroxyl
537 absorption band. Their lower albedo differs from the western Oppia ejecta blanket, making its
538 spectral characteristics more similar to the most common dark hydrated materials found on Vesta.
539 The moderate spectral slope could be due to some photometric effect sensitive to freshness and
540 grain size of the regolith.

541 ## 5. Conclusions

542 We have performed a new analysis of the VIR spectral dataset that includes upgrades of the flat field
543 and response function of the instrument, along with implementing the Shkuratov phase function in
544 the photometric correction. Then we computed global and quadrangle maps of the 1.4 μm
545 reflectance and 2.8 μm band depth, as part as the common set of products used in this special issue

546 of Icarus on Vesta Surface Composition by Dawn (McCord and Scully, 2015, this issue) We then
547 focused on the interpretation of spectral properties and distribution of dark materials and hydrated
548 materials. As a complement to characterizing the spectral shape, we also calculated the spectral slope
549 between 0.4 and 2.5 μm.
550 The final products (global and polar maps) from this refined dataset show significant improvements
551 with respect to previous publications (De Sanctis et al., 2012; McCord et al., 2012; Turrini et al.,
552 2014), since artifacts such as calibration residuals and seams between individual images in the
553 mosaics are minimized. These results alone are a way to validate the choice of techniques and
554 methodologies that we developed. However, VIR IR spectra are not completely explained, partly
555 because our photometric correction assumes one single phase function, which implies homogeneity
556 of physical properties (roughness, porosity) at large scales. Future improvements shall include
557 variations of photometric properties across the surface of Vesta. Furthermore, spectra of the
558 Shkuratov phase function global parameters exhibit a change of regime at 2.5 μm where reflectance
559 fluctuations fall outside photometric model predictions. Possible temporal variations have to be
560 investigated, including changes in the instrument responsivity, effects of temperature of Vesta's
561 regolith, and fluctuations of hydrated material content at the surface.
562 Another innovation is the simultaneous representation of two parameters based on a two-dimension
563 color table, which enhances data that deviate from the general trend. This approach is adequate
564 when two parameters are correlated, and the use of colors in a two-parameter scatter plot allows the
565 simultaneous description of certain spectral properties and their localization on Vesta.
566 The main scientific outcomes are the identification of new properties of certain surface units of
567 Vesta. The region that includes the Bellicia, Arruntia and Pomponia craters contains some hydrated
568 materials with a relatively high albedo (Combe et al., 2015, this issue), while Oppia's western ejecta
569 blanket have similar properties but different types of hydroxyl absorption bands (Tosi et al., 2015,
570 this issue). Variations of spectral slope compared to the distribution of hydrated materials indicates
571 possible effects of coating in small areas such as ejecta blankets and ejecta rays of small, fresh impact
572 craters, although this interpretation is merely a hypothesis at this stage. Further analysis of the
573 physical properties of the regolith could be performed from calculation of photometric parameters,
574 which are sensitive to the surface roughness (e.g. Hapke, 1981; 2002; Muinonen et al., 2002; Shepard
575 and Helfenstein, 2007, 2011; Helfenstein and Shepard, 2011; Souchon et al., 2011; Deb and Sen,
576 2012; Johnson et al., 2013) and the porosity of the surface (Hapke, 2008, Helfenstein and Shepard,

577 2011), and thermal inertia, which is also a function of the porosity of the surface, such as exposed
578 rock vs. soil (Jakosky, 1986; Capria et al., 2014).

579 Acknowledgments

580 We thank David Blewett and an anonymous reviewer for helping improving the manuscript, and
581 Jennifer Scully and Sharon Uy for their editing assistance. Dawn datasets are publicly available at the
582 Planetary Data System Small Bodies Node (http://pdssbn.astro.umd.edu/).
583 The funding for this research was provided under the NASA Dawn mission through a subcontract
584 2090-S-MB516 from the University of California, Los Angeles. The VIR instrument and VIR team
585 are funded by ASI (Italian Space Agency) and INAF (Istituto Nazionale di Astrofisica).

References

Acton, C.H.; "Ancillary Data Services of NASA's Navigation and Ancillary Information Facility;" Planetary and Space Science, Vol. 44, No. 1, pp. 65-70, 1996.

Akimov, L. A. 1975. The effect of mesorelief on the brightness distribution across a planet. Astronomicheskii Zhurnal, vol. 52, May-June 1975, p. 635-641. Soviet Astronomy, vol. 19, no. 3, 1976, p. 385-388. Translation.

Ammannito E., de Sanctis M. C., Palomba E., Longobardo A., Mittlefehldt D. W., McSween H. Y., Marchi S., Capria M. T., Capaccioni F., Frigeri A., Pieters C. M., Ruesch O., Tosi F., Zambon F., Carraro F., Fonte S., Hiesinger H., Magni G., McFadden L. A., Raymond C. A., Russell C. T., Sunshine J. M., 2013a, Olivine in an unexpected location on Vesta's surface, Nature, Volume 504, Issue 7478, pp. 122-125 , doi: 10.1038/nature12665.

Ammannito E., De Sanctis M.-C. , Capaccioni F., Teresa Capria M., Carraro F., Combe J.-Ph., Fonte S., Frigeri A., Joy S. P., Longobardo A., Magni G., Marchi S., McCord T. B., McFadden L. A., McSween H. Y., Palomba E., Pieters C. M., Polanskey C. A., Raymond C. A., Sunshine J. M., Tosi F., Zambon F., Russell C. T., 2013b, Vestan lithologies mapped by the visual and infrared spectrometer on Dawn, Meteoritics & Planetary Science, Volume 48, Issue 11, pp. 2185-2198., doi: 10.1111/maps.12192.

Capria, M. T.; Tosi, F.; De Sanctis, M. C.; Capaccioni, F.; Ammannito, E.; Frigeri, A.; Zambon, F.; Fonte, S.; Palomba, E.; Turrini, D.; Titus, T. N.; Schröder, S. E.; Toplis, M.; Li, J.-Y.; Combe, J.-P.; Raymond, C. A.; Russell, C. T., 2014, Vesta surface thermal properties map, Geophysical Research Letters, Volume 41, Issue 5, pp. 1438-1443, doi: 10.1002/2013GL059026.

Cloutis, Edward A.; McCormack, Kaitlyn A.; Bell, James F.; Hendrix, Amanda R.; Bailey, Daniel T.; Craig, Michael A.; Mertzman, Stanley A.; Robinson, Mark S.; Riner, Miriam A., 2008, Ultraviolet spectral reflectance properties of common planetary minerals, Icarus 197, 321-347, doi: 10.1016/j.icarus.2008.04.018.

Cloutis, E. A.; Izawa, M. R. M.; Pompilio, L.; Reddy, V.; Hiesinger, H.; Nathues, A.; Mann, P.; Le Corre, L.; Palomba, E.; Bell, J. F., 2013, Spectral reflectance properties of HED meteorites + CM2 carbonaceous chondrites: Comparison to HED grain size and compositional variations and implications for the nature of low-albedo features on Asteroid 4 Vesta, Icarus, 223, 850-877, doi: 10.1016/j.icarus.2013.02.003.

Combe J.-Ph., McCord T. B., McFadden L. A., Ieva S., Tosi F., Longobardo A., Frigeri A., De Sanctis M. C., Ammannito E., Ruesch O., Palomba E., Raymond C. A., Russell C. T., 2015, Dawn at Vesta: Composition of the northern regions, Icarus, this issue

Conel, J.E., Green, R.O., Vane, G., Bruegge, C.J., and Alley, R.E. (1987), AIS-2 radiometry and a comparison of methods for the recovery of ground reflectance. In Proceedings of the Third Airborne Imaging Spectrometer Data Analysis Workshop (G. Vane, Ed.), JPL Publ. 87-30, Jet Propulsion Laboratory, Pasadena, CA, pp. 18-47.

De Sanctis, M. C.; Coradini, A.; Ammannito, E.; Filacchione, G.; Capria, M. T.; Fonte, S.; Magni, G.; Barbis, A.; Bini, A.; Dami, M.; Ficai-Veltroni, I.; Preti, G., 2011, The VIR Spectrometer, Space Science Reviews, Volume 163, Issue 1-4, pp. 329-369, doi: 10.1007/s11214-010-9668-5

De Sanctis, M.C., Combe, J.-P., Ammannito, E., Palomba, E., Longobardo, A., McCord, T.B., Marchi, S., Capaccioni, F., Capria, M.T., Mittlefehldt, D.W., Pieters, C.M., Sunshine, J., Tosi, F., Zambon, F., Carraro, F., Fonte, S., Frigeri, A., Magni, G., Raymond, C.A., Russell, C.T., Turrini, D., 2012a, Detection of widespread hydrated materials on Vesta by the VIR imaging spectrometer on voard the Dawn mission. The Astrophysical Journal 758, L36. doi:10.1088/2041-8205/758/2/L36

De Sanctis, M.C., Ammannito, E., Capria, M.T., Tosi, F., Capaccioni, F., Zambon, F., Carraro, F., Fonte, S., Frigeri, A., Jaumann, R., Magni, G., Marchi, S., McCord, T.B., McFadden, L.A., McSween, H.Y., Mittlefehldt, D.W., Nathues, A., Palomba, E., Pieters, C.M., Raymond, C.A., Russell, C.T., Toplis, M.J., Turrini, D., 2012b. Spectroscopic Characterization of Mineralogy and Its Diversity Across Vesta. Science 336, 697–700. doi:10.1126/science.1219270.

De Sanctis M. C.; Ammannito E.; Capria M. T.; Capaccioni F.; Combe J.-Ph.; Frigeri A.; Longobardo A.; Magni G.; Marchi S.; McCord T. B.; Palomba E.; Tosi F.; Zambon F.; Carraro F.; Fonte S.; Li J.-Y.; McFadden L. A.; Mittlefehldt D. W.; Pieters C. M.; Jaumann R.; Stephan K.; Raymond C. A.; Russell C. T., 2013, Vesta's mineralogical composition as revealed by the visible and infrared spectrometer on Dawn, Meteoritics & Planetary Science, 48, 2166-2184, 10.1111/maps.12138.

Deb, D.; Sen, A. K., 2012, Light Scattering from Regolith: Intensity Versus Particle Size Behavior, Earth, Moon, and Planets, Volume 108, Issue 2, pp.101-109, doi: 10.1007/s11038-011-9384-5.

Frigeri et al., 2015, this issue

Gaffey, M.J., 1997. Surface lithologic heterogeneity of asteroid 4 Vesta. Icarus 127, 130–157.

647 Gounelle, M., Zolensky, M. E., Liou, J.-C., Bland, P. A., & Alard, O., 2003, Geochim.
648 Cosmochim. Acta, 67, 507.
649 Hapke B., 1981, Bidirectional reflectance spectroscopy: 1. Theory, J. Geophys. Res., 86,
650 3039–3054.
651 Hapke B., 1993, Theory of reflectance and emittance spectroscopy, Topics in remote sensing
652 3, Cambridge University press, ISBN 0-521-61927-0.
653 Hapke B, 2001, Space weathering from Mercury to the asteroid belt, Journal of Geophysical
654 Research, 106, 10039-10074, doi: 10.1029/2000JE001338.
655 Hapke, B., 2002, Bidirectional reflectance spectroscopy, 5: The coherent backscatter
656 opposition effect and anisotropic scattering, Icarus, 157, 523–534.
657 Hapke, B., 2008. Bidirectional reflectance spectroscopy. 6. Effects of porosity. Icarus 195,
658 918–926.
659 Helfenstein P. and Shepard M. K., Testing the Hake photometric model: Improved
660 inversion and the porosity correction, doi: 10.1016/j.icarus.2011.07.002.
661 Jakosky B. M, 1986, On the thermal properties of Martian fines, Icarus 66, April 1986, 117-
662 124, doi: 10.1016/0019-1035(86)90011-4.
663 Jaumann, R.; Nass, A.; Otto, K.; Krohn, K.; Stephan, K.; McCord, T. B.; Williams, D. A.;
664 Raymond, C. A.; Blewett, D. T.; Hiesinger, H.; Yingst, R. A.; De Sanctis, M. C.; Palomba, E.;
665 Roatsch, T.; Matz, K.-D.; Preusker, F.; Scholten, F.; Russell, C. T., 2014, The geological nature
666 of dark material on Vesta and implications for the subsurface structure, Icarus, 240, 3-19, doi:
667 10.1016/j.icarus.2014.04.035.
668 Johnson, Jeffrey R.; Shepard, Michael K.; Grundy, William M.; Paige, David A.; Foote,
669 Emily J., 2013, Spectrogoniometry and modeling of martian and lunar analog samples and
670 Apollo soils, Icarus, Volume 223, Issue 1, p. 383-406, doi: 10.1016/j.icarus.2012.12.004.
671 Le Corre, L. et al., 2013. Olivine or impact melt: Nature of the “orange” material on Vesta
672 from Dawn. Icarus 226, 1568–1594.
673 Longobardo, Andrea; Palomba, Ernesto; Capaccioni, Fabrizio; De Sanctis, Maria Cristina; Tosi,
674 Federico; Ammannito, Eleonora; Schröder, Stefan E.; Zambon, Francesca;Raymond, Carol A.;
675 Russell, Christopher T.; 2014, Photometric behavior of spectral parameters in Vesta dark and bright
676 regions as inferred by the Dawn VIR spectrometer, Icarus, 240, 20-35
677 Longobardo et al., 2015, Icarus, this issue

678 McCord, Thomas B.; Adams, John B.; Johnson, Torrence V., 1970, Asteroid Vesta: Spectral
679 Reflectivity and Compositional Implications, Science, Volume 168, Issue 3938, pp. 1445-1447,
680 doi: 10.1126/science.168.3938.1445
681 McCord, T.B., Li, J.-Y., Combe, J.-P., McSween, H.Y., Jaumann, R., Reddy, V., Tosi, F.,
682 Williams, D.A., Blewett, D.T., Turrini, D., Palomba, E., Pieters, C.M., De Sanctis, M.C.,
683 Ammannito, E., Capria, M.T., Le Corre, L., Longobardo, A., Nathues, A., Mittlefehldt, D.W.,
684 Schröder, S.E., Hiesinger, H., Beck, A.W., Capaccioni, F., Carsenty, U., Keller, H.U., Denevi, B.W.,
685 Sunshine, J.M., Raymond, C.A., Russell, C.T., 2012. Dark material on Vesta from the infall of
686 carbonaceous volatile-rich material. Nature 491, 83–86. doi:10.1038/nature11561
687 McCord and Scully, 2015, this issue.
688 McSween H. Y., Ammannito E., Reddy V., Prettyman T. H., Beck A. W., Cristina de Sanctis
689 M., Nathues A., Corre L., O'Brien D. P., Yamashita N., McCoy T. J., Mittlefehldt D. W., Toplis
690 M. J., Schenk P., Palomba E., Turrini D., Tosi F., Zambon F., Longobardo A., Capaccioni F.,
691 Raymond C. A., Russell C. T., 2013, Composition of the Rheasilvia basin, a window into Vesta's
692 interior, Journal of Geophysical Research118, Issue 2, pp. 335-346, doi: 10.1002/jgre.20057.
693 Muinonen, K.; Piironen, J.; Shkuratov, Yu. G.; Ovcharenko, A.; Clark, B. E., 2002, Asteroid
694 Photometric and Polarimetric Phase Effects, Asteroids III, W. F. Bottke Jr., A. Cellino, P.
695 Paolicchi, and R. P. Binzel (eds), University of Arizona Press, Tucson, p.123-138.
696 Noble, Sarah K.; Pieters, Carlé M.; Taylor, Lawrence A.; Morris, Richard V.; Allen, Carlton
697 C.; McKay, David S.; Keller, Lindsay P., 2001, The optical properties of the finest fraction of
698 lunar soil: Implications for space weathering, Meteoritics & Planetary Science, 36, 31-42, doi:
699 10.1111/j.1945-5100.2001.tb01808.x.
700 Palomba, Ernesto; Longobardo, Andrea; De Sanctis, Maria Cristina; Zambon, Francesca;
701 Tosi, Federico; Ammannito, Eleonora; Capaccioni, Fabrizio; Frigeri, Alessandro; Capria, Maria
702 Teresa; Cloutis, Edward A.; Jaumann, Ralf; Combe, Jean-Philippe; Raymond, Carol A.; Russell,
703 Christopher T., 2014, Composition and mineralogy of dark material units on Vesta, Icarus,
704 Volume 240, p. 58-72, doi: 10.1016/j.icarus.2014.04.040
705 Pieters, C. M.; Ammannito, E.; Blewett, D. T.; Denevi, B. W.; de Sanctis, M. C.; Gaffey, M.
706 J.; Le Corre, L.; Li, J.-Y.; Marchi, S.; McCord, T. B.; McFadden, L. A.; Mittlefehldt, D. W.;
707 Nathues, A.; Palmer, E.; Reddy, V.; Raymond, C. A.; Russell, C. T., 2012, Distinctive space

708 weathering on Vesta from regolith mixing processes, Nature, 491, 79-82, doi:
709 10.1038/nature11534.

710 Prettyman, T.H., Mittlefehldt, D.W., Yamashita, N., Lawrence, D.J., Beck, A.W., Feldman,
711 W.C., McCoy, T.J., McSween, H.Y., Toplis, M.J., Titus, T.N., Tricarico, P., Reedy, R.C.,
712 Hendricks, J.S., Forni, O., Le Corre, L., Li, J.-Y., Mizzon, H., Reddy, V., Raymond, C.A.,
713 Russell, C.T., 2012. Elemental Mapping by Dawn Reveals Exogenic H in Vesta's Regolith.
714 Science 338, 242–246. doi:10.1126/science.1225354.

715 Reddy, V., Le Corre, L., O'Brien, D.P., Nathues, A., Cloutis, E.A., Durda, D.D., Bottke, W.F.,
716 Bhatt, M.U., Nesvorny, D., Buczkowski, D., Scully, J.E.C., Palmer, E.M., Sierks, H., Mann, P.J.,
717 Becker, K.J., Beck, A.W., Mittlefehldt, D., Li, J.-Y., Gaskell, R., Russell, C.T., Gaffey, M.J.,
718 McSween, H.Y., McCord, T.B., Combe, J.-P., Blewett, D., 2012a. Delivery of dark material to Vesta
719 via carbonaceous chondritic impacts. Icarus 221, 544–559. doi:10.1016/j.icarus.2012.08.011.

720 Reddy, V. et al., 2012b. Albedo and color heterogeneity of Vesta from Dawn. Science 336, 700–
721 704.

722 Roatsch, Th.; Kersten, E.; Matz, K.-D.; Preusker, F.; Scholten, F.; Jaumann, R.; Raymond, C. A.;
723 Russell, C. T., 2012, High resolution Vesta High Altitude Mapping Orbit (HAMO) Atlas derived
724 from Dawn framing camera images, Planetary and Space Science, 73, 283-286, doi:
725 10.1016/j.pss.2012.08.021.

726 Schröder, S. E.; Mottola, S.; Keller, H. U.; Raymond, C. A.; Russell, C. T., 2014, Resolved
727 photometry of Vesta reveals physical properties of crater regolith, Planetary and Space Science, 103,
728 66-81, doi: 10.1016/j.pss.2014.08.001.

729 Shepard, M. K.; Helfenstein, P., 2007, A test of the Hapke photometric model, Journal of
730 Geophysical Research, Volume 112, 10.1029/2005JE002625.

731 Shepard M. K. and Helfenstein P., 2011, A laboratory study of the bidirectional reflectance from
732 particular samples, Icarus 2015, 526-533, doi:10.1016/j.icarus.2011.07.033.

733 Shkuratov, Yu. G.; Kreslavsky, M. A.; Ovcharenko, A. A.; Stankevich, D. G.; Zubko, E. S.;
734 Pieters, C.; Arnold, G., 1999, Opposition Effect from Clementine Data and Mechanisms of
735 Backscatter, Icarus, 141, 132-155, doi: 10.1006/icar.1999.6154.

736 Souchon, A. L.; Pinet, P. C.; Chevrel, S. D.; Daydou, Y. H.; Baratoux, D.; Kurita, K.; Shepard,
737 M. K.; Helfenstein, P., 2011, An experimental study of Hapke's modeling of natural granular surface
738 samples, Icarus, Volume 215, Issue 1, p. 313-331, 10.1016/j.icarus.2011.06.023

739 Thekaekara, M. P., 1973, Extraterrestrial solar spectral irradiance, in: The Extraterrestrial Solar
740 Spectrum, edited by: Drummond, A. J. and Thekaekara, M. P., Institute of Environmental Studies,
741 Mot Prospect, IL.
742 Turrini, D.; Combe, J.-P.; McCord, T. B.; Oklay, N.; Vincent, J.-B.; Prettyman, T. H.; McSween,
743 H. Y.; Consolmagno, G. J.; De Sanctis, M. C.; Le Corre, L.; Longobardo, A.; Palomba, E.; Russell,
744 C. T., 2014, The contamination of the surface of Vesta by impacts and the delivery of the dark
745 material, Icarus, Volume 240, p. 86-102, doi: 10.1016/j.icarus.2014.02.021
746 Tosi et al., 2015, this issue
747 Wagner, J. K.; Hapke, B. W.; Wells, E. N., 1987, Atlas of reflectance spectra of terrestrial, lunar,
748 and meteoritic powders and frosts from 92 to 1800 nm, Icarus 69, 14-28, doi: 10.1016/0019-
749 1035(87)90003-0.
750 Williams D. A.; O'Brien D. P.; Schenk P. M.; Denevi B. W.; Carsenty U.; Marchi S.; Scully J. E.
751 C.; Jaumann R.; De Sanctis M. C.; Palomba E.; Ammannito E.; Longobardo A.; Magni G.; Frigeri
752 A.; Russell C. T.; Raymond C. A.; Davison T. M., 2014, Lobate and flow-like features on asteroid
753 Vesta, Planetary and Space Science, 103, 24-35, doi: 10.1016/j.pss.2013.06.017.
754 Zambon, F.; De Sanctis, Maria Cristina; Schröder, Stefan; Tosi, Federico; Longobardo, Andrea;
755 Ammannito, Eleonora; Blewett, David T.; Mittlefehldt, David W.; Li, Jian-Yang; Palomba, E.;
756 Capaccioni, Fabrizio; Frigeri, Alessandro; Capria, Maria Teresa; Fonte, Sergio; Nathues, Andreas;
757 Pieters, Carle M.; Russell, Christofer T.; Raymond, Carol A., 2014, Spectral analysis of the bright
758 materials on the asteroid Vesta, Icarus, Volume 240, p. 73-85, doi: 10.1016/j.icarus.2014.04.037
759 Zambon et al., 2015, Icarus this issue
760 Zolensky, M. E., Weisberg, M., Buchanen, P. C., & Mittlefehldt, D. W. 1996, Meteorit.
761 Planet. Sci., 31, 518
762
763

Appendix: Partial derivatives of the Shkuratov phase function H

Definition of the Shkuratov phase function:

$$H(\alpha) = \frac{\exp(-k\alpha)}{2 + exp\left(\frac{-d}{L}\right)}\left[2 + \frac{exp\left(\frac{-d}{L}\right)}{\sqrt{1 + \left(\frac{4\pi L}{\lambda}\sin\frac{\alpha}{2}\right)^2}}\right]$$

where

$$k = k_0(1 - A)$$

1) Partial derivative with respect to k_0:

$$\frac{\partial H(\alpha)}{\partial k_0} = (A - 1) \times \alpha H(\alpha)$$

2) Partial derivative with respect to A:

$$\frac{\partial H(\alpha)}{\partial k_0} = \frac{1 + \alpha A k_0}{A H(\alpha)}$$

3) Partial derivative with respect to d:

$$Z = A \times \exp[-\alpha k_0(1 - A)]$$

$$S = \sqrt{1 + [4\pi L/\lambda \times \sin(\alpha/2)]^2}$$

$$U = -d/L$$

$$X = 2 + \exp(U)$$

$$V = \exp(U)$$

$$U_p = -1/L$$

$$X_p = U_p \exp(U)$$

$$W = \frac{-ZX_p}{X^2}$$

$$\frac{\partial H(\alpha)}{\partial d} = W(2 + V/S) + \frac{Z}{X}\frac{X_p}{S}$$

4) Partial derivative with respect to L:

$$Z = A \times \exp[-\alpha k_0(1 - A)]$$

789 $S = 4\pi/\lambda \times \sin(\alpha/2)$

790 $U = -d/L$

791 $X = 2 + \exp(U)$

792 $V = \exp(U)$

793 $T = 1 + (YL)^2$

794 $W = \sqrt{T}$

795 $U_p = \frac{d}{L^2}$

796 $X_p = U_p \exp(U)$

797 $P = ZX_p/X^2$

798 $T_p = 2LY^2$

799 $W_p = \frac{T_p}{2\sqrt{T}}$

800 $Q = WX_p - VW_p/W^2$

801

802 $$\frac{\partial H(\alpha)}{\partial L} = P(2 + V/W) + \frac{Z}{X}Q$$